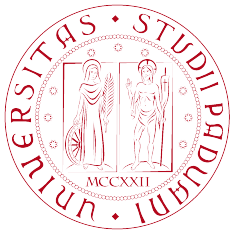

UNIVERSITÀ DEGLI STUDI DI PADOVA

DIPARTIMENTO DI INGEGNERIA INDUSTRIALE
Corso di Laurea Magistrale in Ingegneria Aerospaziale

ON THE UNCERTAINTY QUANTIFICATION OF THE UNSTEADY AERODYNAMICS OF 2D FREE FALLING PLATES

Relatore:
Prof. Giampaolo Navarro

Correlatori:
Prof. Marco Antonello
Prof. José Carlos Fernandes Pereira

Laureando:
Nicola Zorzi
Matricola 1015071

Anno Accademico 2013-2014

This thesis is dedicated to my parents
for their love, endless support
and encouragement

Sommario

In questa tesi si è studiato numericamente la caduta libera di piastre bidimensionali in un fluido utilizzando un approccio numerico sia per quanto riguarda le soluzioni deterministiche sia per quelle stocastiche. Il moto è caratterizzato dall'interazione tra fluido e corpo descritta attraverso l'interazione delle equazioni di Navier-Stokes e quelle della dinamica del corpo rigido. Le previsioni del modello sono state comparate con i dati disponibili in letteratura.
Nelle simulazioni stocastiche, il raggio di curvatura della lastra è stato considerato come variabile aleatoria caratterizzata da una funzione di densità di probabilità (PDF) uniforme. In questo modo sono state introdotte delle incertezze direttamente nei risultati che sono state quantificate attraverso un metodo non intrusivo (Non-Intrusive Spectral Projection) basato sulla teoria del caos polinomiale. L'analisi si è concentrata sul calcolo della traiettoria mediana e la relativa barra di errore per entrambi i casi di tumbling e fluttering.

Parole chiave: Falling plate · Fluttering · Tumbling · Incertezza · Analisi stocastica

Abstract

The free fall of two-dimensional cards immersed in a fluid was studied using a deterministic and stochastic numerical approach. The motion is characterized by the fluid-body interaction described by coupling the Navier-Stokes and rigid body dynamic equations. The model's predictions have been validated and using both the experimental and numerical data available in literature.
In the stochastic simulations, the fillet radius of the plate was considered a random variable characterized by a uniform Probability Density Function (PDF) introducing, in this way, some uncertainties in the plate's trajectory. To take into account the uncertainties we employed the Non-Intrusive Spectral Projection (NISP) method based on polynomial chaos expansion. The analysis was focused on finding the ensemble mean trajectory and error bar for a confidence interval of 95% for both tumbling and fluttering regimes.

Keywords: Falling plate · Fluttering · Tumbling · Uncertainty Quantification · Stochastic analysis

CONTENTS

LIST OF FIGURES

LIST OF TABLES

NOMENCLATURE

Latin Symbols

AR	Aspect ratio
$\boldsymbol{F}$	Resultant force acting on the plate
f	Stochastic solution
$\hat{f}$	Deterministic solution
g	Acceleration due to gravity
Ga	Galilei dimensionless number
H_a	High of the computational domain above the plate
H_b	High of the computational domain below the plate
h	Plate thickness
$\mathcal{I}$	Tensor of the moments of inertia of the rigid body
$\mathcal{J}$	Second moment of area
J	Impulse of a force
l	Plate length
$\boldsymbol{M}$	Fluid torque
m	Mass of the body
P	Probability
p	Pressure
R	Radius of the inner circle of the computational domain
Re	Reynold's number
r	Fillet radius
t	Time
$\mathcal{S}$	Region of the profile
s	Mesh thickness of the computational model
$\boldsymbol{u}$	Fluid velocity
U_t	Average descending velocity
$\boldsymbol{v}$	Velocity of the centre of mass of the falling body
W	Width of the geometrical domain

Greek Symbols

ϑ	Body inclination
ν	Kinematic viscosity
ξ	Random variable associated with the uncertain parameter
ρ	Density
φ_n	Orthogonal polynomial number n
$\boldsymbol{\omega}$	Angular velocity of the rigid body

Subscripts

b	Body
f	Fluid
i	Vector component
x	Component in the x axes

y Component in the y axes
0 Initial condition

Superscript

$*$ Dimensionless parameter

ACRONYMS

CFD Computational Fluid Dynamics
branch of fluid mechanics that uses numerical methods and algorithms to solve and analyse problems that involve fluid flows.

ISP Intrusive Spectral Projection
uncertainty quantification method that quantifies the confidence interval by the reformulation of the governing equations.

NISP Non-Intrusive Spectral Projection
uncertainty quantification method that uses deterministic solutions in order to quantify their confidence interval.

PDF Probability Density Function
function that describes the relative likelihood for a random variable to take a given value.

SIMPLE Semi-Implicit Method for Pressure-Linked Equations
predictor corrector algorithm used in the solution of the equations to link velocity and pressure.

2D Two-dimensional

1 INTRODUCTION

Every one must have observed that when a slip of paper falls through the air, its motion, through undecided and wavering at first, sometimes become regular.

James Clerk Maxwell (1831-1879)

1.1 MOTIVATION

The dynamic behaviour of free falling objects in a fluid is particularly interesting through an aerodynamic point of view. In its generality, the final motion is the result of a series of complicated phenomena: lift, drag, stall, wake instability, vortex shedding and fluid-body interactions are just a few examples of what one has to consider when studying the free fall. These considerations can find direct application in several areas and problems such as firebrands transportation in forest fires [1], insect flight [2], fall of plant seeds [3–5], design of micro air vehicle for both civil and military purposes [6], prediction of small particles sedimentation [7] or fall of barks.
As a results, the analysis of free falling plates can be a valid way for applying and deepening the theoretical knowledges in which important fluid dynamics aspects are joined together.

1.2 OBJECTIVE

The objective of the study is to investigate the role that geometrical uncertainties play on the motion of falling objects. The general physics is characterized by the presence of vortices which shed at the trailing edge interacting with the body. As a result, the associated fluid dynamics can be complex enough to make the theoretical treatment difficult, justifying the numerical approach.
The first aim is to find with the commercial software STAR-CCM+ a good agreement with the literature results in order to consider the best mesh for the further simulations. Afterwards, we are interested in finding the uncertainties quantification for an input stochastic variable, that is, the edge fillet radius of the plate. Since the code of the commercial software is closed, it is not possible to handle and modify the governing equations introducing a stochastic variable, so, deterministic solutions will be calculated and the uncertainty analysis will be carry out *a posteriori* through the Non-Intrusive Spectral Projection (NISP) method. The two characteristic free fall motions, tumbling and fluttering, will be considered in the further analysis.

1.3 FREE FALL – LITERATURE SURVEY

We all know that a falling leaf does not reach the ground with a straight vertical trajectory but a graceful and elegant path is drawn in the air. Similarly, tree seeds, business cards, or common sheets of paper, fall down oscillating from side to side (fluttering), drifting sidewise and spinning through an axis (tumbling), or they can also have more complicated three dimensional motions, such as autogyration and rolling autogyration, or simply, they can fall down with a particular combination of the previous modes [8].

The study of falling strips of paper started with Maxwell in 1854 [9], even before the development of the aerodynamic theory, with a qualitative description of the tumbling phenomena. He attributed the sustained rotation to the air resistance that produces moment. He observed how the motion becomes stable only if the rotation takes place along the major axis of the rectangular piece of paper and its path will be straight only if this axis is aligned with the horizon. On the contrary, rectangular bodies with horizontal inclination or elongated trapezoids will always have helicoidal trajectories. Later, Mouillard [10] gave an explanation for the tumbling motion in rectangular plates distinguishing the centre of pressure and the geometrical centre while Riabouuchinsky [11] concentrated on the main differences between fixed (auto-rotation) and freely moving axes (free fall). Later, Dupleich [12] carried out a big number of experiments (both in air and in water) trying to quantify mathematically, in an average manner, the motion characteristics for several body shapes dropped in different conditions. In particular he studied the motion of prisms (including rectangular section plates), paddle wheels, cylinders, curved wings and isosceles trapezoids. Regarding the launching conditions, he dropped the objects from auxiliary platforms, motors or directly by hands. He recognized that in some specific geometrical conditions, rotation is impossible and periodic-oscillating motion (fluttering) appears. In 1964, Willmarth *et al.* [13] observed the three-dimensional fall of circular disks finding a wide variety of types of motion: tumbling, steady-falling, fluttering and an apparently chaotic motion. In addition, he explained how the transition between these regimes is governed by the dimensionless moment of inertia, $\mathcal{I}^*$.

Smith [14] conducted a series of experiences focusing on autogyration and tumbling (free fall) of a rectangular plate using an aspect ratio varying between 3 to 4. He recognized how the phenomena is governed by three dimensionless numbers: the Reynold's number, the dimensionless moment of inertia and the aspect ratio. By the auxiliary of a wind tunnel he was able to study the flow around the plate and quantify the unsteady lift, drag, angular acceleration and the rotation rate (for fixed axis). Regarding free falling plates a dependence on the Reynold's number was observed. Lugt [15, 16] conducted both experimental and numerical research solving the flow equations with the potential-flow theory recognizing the big role played by the vortex shedding. He studied the behaviour of various bodies immersed in air which have free or fixed moving axis. These authors (Smith and Lugt) tried to relate the similarities between freely falling and fixed axis auto-rotation plates but the two phenomena are substantially different. Just think about the degrees of freedom involved in the two cases: in the fixed axis only the rotation is considered as variable. Therefore, no coupling with translation is taken into account.

Concerning the free falling research, Field *et al.* [17] study experimentally the free fall of circular disks made of steal and lead. Disks with different

diameters and thicknesses were dropped in water/glycerol mixture. An investigation on the dependency on the dimensionless numbers of Reynold and dimensionless moment of inertia was conducted and the experimental results were reported in a plot (Re *vs* $\mathcal{I}^*$) distinguishing 4 regions, each one with a different kind of motion (steady falling, periodic oscillations, chaotic motion and tumbling). Chrust *et al.* [18] basically reproduced these results using a numerical approach.
Mahadevan *et al.* [19] relate experimentally the tumbling frequency with the dimensions (length l, width w and thickness t) of rectangular cards which satisfy the relationship $l \gg w \gg t$ trying, in this way, to eliminate three dimensional effects. In 1998, Belmonte *et al.* [20] studied the transition from fluttering to tumbling in a quasi-two-dimensional experiment in which flat strips were dropped in a narrow container filled with fluid (water, glycerol/water or petroleum ether) and mechanical constraints ensured the two-dimensional plate motion. Further improvements were done by Andersen *et al.* [21] who eliminated the mechanical constrained and used a release mechanism for dropping the aluminium plates. By using a high-speed digital video camera they determined the instantaneous acceleration and thus the instantaneous forces acting on the plate. In 2013, Varshney *et al.* [22] have investigated the motion of falling parallelograms that exhibit coupled motion of autogyration and tumbling. With the auxiliary of a high-speed camera, a kinematic and dynamic analysis have been conducted finding, in this way, the various forces acting on the body.
In the last decade, free falling has been investigated using Computational Fluid Dynamics (CFD). In general, numerical simulation of freely falling body is not a simple problem: it requires models with unsteady aerodynamics and moving solid boundaries and, because of large integration time if compared with the time step, a comprehensive analysis needs large computational capacities. In addition, it needs to study the fluid-body interaction: the plate is considered perfectly rigid but the trajectory is the result of the combined action of both the fluid forces and the gravitational ones. In this direction Mittal *et al* [23] solve directly the Two-dimensional (2D) Navier-Stokes equations for both fixed and free axes plate. In this analysis, it was found that the plate has an increase tendency to tumble when the Reynolds number increases and the thickness ratio decreases. In addition, it seems that the tumbling frequency is governed by a Karman type vortex shedding process. Pesavento & Wang [24] solved the 2D Navier-Stokes equations for the flow around tumbling plate in the vorticity stream function formulation using a body-fixed elliptical coordinate system. For the resolution a conformal mapping was used and, to avoid singularities, an elliptical cross section plate was modelled. Andersen *et al.* [21], using the same mathematical formulation, qualitatively compared the numerical solution, for tumbling and fluttering cases, with the experimental one measured in the same paper and ascribed the discrepancies to the differences in geometry between the rectangular cross-section in experiment and the elliptical one in numerical simulation. In [25], the same authors conduct a series of numerical simulations in air and solved numerically the free fall governing differential equations. They discussed the transition between tumbling and fluttering and concluded that the transition is a heteroclinic bifurcation and suggested that the apparently chaotic motion observed in the experiments is due to the high sensitivity to experimental noise. Later, in 2008, Jin & Xu [26] try to overcome the various discrepancies between experimental and numerical solution encountered in the first work of Andersen *et al.* ([21]). Using a gas-

kinetic scheme, the 2D Navier-Stokes equations are solved on a moving grid. They found a good agreement with the experimental results remarking that the main difference between the elliptical and rectangular cross-section is the angular velocity, in which the elliptical one rotates much faster.
In this field, authors concentrate their attention on the understanding and prediction of the various regimes and many efforts are done to map the various regions in which the specific motion appears. In this context, in the numerical simulation, the body shape is considered ideal, and no uncertainties in the input parameters are taken into account. In this work we consider a geometry uncertainty, the fillet radius, and, through the simulations conducted with a commercial software and the further application of the NISP the mean trajectory and the relative confidence interval are calculated.

1.4 THESIS OUTLINE

This work has the following organization. Besides this chapter which includes an introduction of free falling plates as well as the motivation and the objective of this work, the next chapter is dedicated to the problem definition. It will be defined starting from the governing equations in which follow the computational domain as well as the boundary conditions considered. Will also be briefly described the finite volume method for unstructured mesh and the numerical discretization used by STAR-CCM+ for time, convection and diffusive terms. Finally, a short description of both SIMPLE method used for the pressure-velocity coupling and the algorithm to solve linear system of equation will be done.
Chapter 3 is dedicated to the validation and verification study. The model mesh will be reported and the results will compared with the literature ones and a critical and detailed discussion will be performed.
Chapter 4 starts with a short introduction of the NISP method in which follows its mathematical formulation. Finally, stochastic analysis will be performed to both tumbling and fluttering plate and results will be discussed.
The last chapter summarizes the most important conclusions reached with this analysis.

2 NUMERICAL PROCEDURE

Everything should be made as simple as possible, but not simpler.

Albert Einstein (1879-1955)

This chapter is dedicated to the numerical procedure used. Since the system is characterized by a fluid-body interaction, both the rigid body dynamic equations and the fluid equations are shown. Afterwards, will be reported the computational domain and its boundary conditions will be discussed. Will also be briefly described the finite volume method for unstructured mesh as well as the numerical discretization for time, convection and diffusive terms adopted by the commercial software used. Finally a short description of both the pressure-velocity coupling used to solve the equation – Semi-Implicit Method for Pressure-Linked Equations (SIMPLE) method – and the algorithm used to solve large linear system of equations will be reported.

2.1 EQUATIONS OF MOTION

The motion of 2D free falling plates is governed by six independent variables [14], *i.e.*, the length of the plate l, its thickness h, the fluid density ρ_f, the body density ρ_b, the kinematic viscosity ν and the acceleration due to gravity g. By conducting dimensional analysis (for more details see Appendix A) it is possible to restrict the analysis to three dimensionless quantities: the aspect ratio AR, the solid to fluid density ratio ρ_s/ρ_f and the Galilei number $\mathrm{Ga} = \sqrt{l^3 g}/\nu$. In any case, the body is subjected to both the force due to gravity and the hydrodynamic force. Therefore, in the following, the basic flow equations as well as the rigid body equations will be presented.

2.1.1 Flow Equations

In order to find the fluid dynamical forces it is necessary to know the pressure field around the plate, i.e. we need to solve the flow equations. The free falling objects considered in this analysis are characterized by small body velocities (always less than $1\,\mathrm{m\,s^{-1}}$) that imply small Mach numbers. In this way the fluid can be treated as incompressible and this simplifies a lot the mathematical formulation. In addition, since the plate is supposed to fall in air or in water, Newtonian fluid is considered. The flow governing equations are the continuity and the Navier-Stokes equations that, for the two-dimensional case are:

$$\nabla \cdot \boldsymbol{u} = 0 \qquad \frac{\partial \boldsymbol{u}}{\partial t} + (\boldsymbol{u} \cdot \nabla)\,\boldsymbol{u} = -\frac{1}{\rho}\nabla p + \nu \nabla^2 \boldsymbol{u} \tag{1}$$

where u is the velocity, t is the time, p is the static pressure, ρ is the density and ν is the kinematic viscosity.

The motion is characterized by a Reynold's number up to 6000, value that is much lower than the critical Reynold's number for plates in external flow ($\mathrm{Re}_c \approx 2 \times 10^5$, see [27]): laminar flow is therefore considered.

2.1.2 Rigid Body Equations

The body motion is governing by the cardinal equations of dynamics. The translation of the centre of mass has the following differential equation, formulated in the global inertial reference system:

$$\boldsymbol{F} = m\frac{\mathrm{d}\boldsymbol{v}}{\mathrm{d}t} \tag{2}$$

where m is the mass (considered constant), $\boldsymbol{v}$ is the velocity of the centre of mass and $\boldsymbol{F}$ is the resultant force acting on the body that is the sum of the buoyancy, the gravity and the hydrodynamics forces.
The equation of rotation of the body is expressed in the body local coordinate system with the origin in the centre of mass:

$$\boldsymbol{M} = \mathcal{I}\dot{\boldsymbol{\omega}} + \boldsymbol{\omega} \times \mathcal{I}\boldsymbol{\omega} \tag{3}$$

where $\boldsymbol{\omega}$ is the angular velocity of the rigid body, $\boldsymbol{M}$ is the resultant moment acting on the body (due to fluid forces) and $\mathcal{I}$ is the tensor of the moments of inertia. However, because of the 2D nature of this analysis, $\boldsymbol{\omega} = \omega\hat{\boldsymbol{\imath}}_z$ and therefore $\boldsymbol{M} = M\hat{\boldsymbol{\imath}}_z$, equation (3) can be expressed as follows:

$$M = \mathcal{I}_{zz}\dot{\omega} \tag{4}$$

where a reference frame with its axes parallel to the body's principal axis of inertia is considered.

2.2 GEOMETRICAL MODEL AND BOUNDARY CONDITIONS

In order to simulate the free fall of a plate, the sliding mesh method will be used. It consists on a floating object fixed on a disk that can rotate with respect the rest of the mesh. This approach is particularly suitable for free falling object because larger rotating angles will be evolved and a fine mesh restricted only in the disk region is required. The geometrical model is represented in Figure 1. Here the fluid region is composed by two different parts: the internal rotating disk and the external mesh that can only translate. To construct a universal domain for different plates geometry, all dimensions are proportional to a characteristic one, that is the plate length l.

The two-dimensional motion was modelled using a one-cell-thick three dimensional mesh instead of a true two-dimensional mesh: this choice was imposed by the software used, in which rigid body motions can only be simulated using a three-dimensional mesh.
Beside that, no significantly losses in computational efficiency has been noted.

Regarding the boundary conditions, we have:

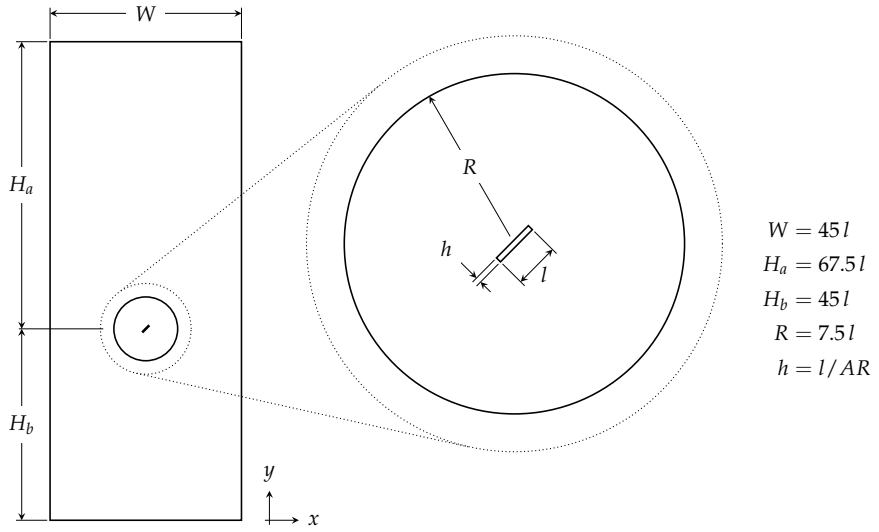

Figure 1.: Computational domain. On the left a representation of the full domain is shown while on the right side a zoom of the internal disk is done. In addition, the figure reports the values of the various dimensions, all expressed in term of the plate length l.

WALL Due to the friction effects, the fluid in contact with the wall has no relative velocity with boundary (no-slip condition), so it is a Dirichlet boundary condition. It is applied to the body-fluid interface.

INLET In this case the inlet face velocity vector is specified directly. Since the computational domain is not fixed the velocity vector is not zero in the non rotating frame of reference fixed on the card. Nevertheless, in the global coordinate system, sufficiently far from the plate, the fluid stays at rest so $0\,\mathrm{m\,s^{-1}}$ is imposed. It is applied to the bottom and lateral faces of the computational domain.

OUTLET The pressure is specified. Sufficiently far the fluid is not influenced by the plate's wake. Value of 0 Pa is imposed. Top face of the domain has this kind of boundary condition.

INTERFACE This is the boundary condition that allows the sliding mesh method. It is applied to the interface between the inner circle and the outer rectangular. The two surfaces are temporarily directly joined and an unique region without physical separation in space is created. Afterwards, in the following time-step, an upgrade of the relative position between each other as well as a new temporarily union will be done.

SYMMETRY PLANE A symmetry plane boundary consist to put an imaginary plane of symmetry in the simulation. The solution that is obtained is identical to the one that would be obtained by mirroring the mesh about the symmetry plane. This condition is applied both to the forward and the backward surface of the computational domain and it is fundamental to perform two-dimensional simulations.

2.3 STAR-CCM+ NUMERICAL MODEL

2.3.1 Finite-Volume Method and Unstructured Mesh

The finite-volume method is a discretization technique that is extensively used in CFD. The computational domain is subdivided into a finite number of small control volumes in which the various physical proprieties are considered constant. In contrast to the finite difference method, which defines the computational nodes, finite volume technique defines the control volume boundaries and only afterwards, will be assigned the computational node to the control volume centre. Since its introduction (1971), this method has been intensely used for basically two reasons: first, it ensures that the discretization is conservative or, in other words, the conservative laws are satisfied at the discrete level, and second, it does not require any coordinate transformation so it can be applied directly on irregular meshes. Therefore, it finds an application in meshes consisting of arbitrary polyhedra (or polygons, in two-dimensions). This kind of mesh, also called *unstructured* mesh, is very suitable because automatic grid generation codes can be used efficiently for complex geometries. For a comprehensive analysis see for example [28] or [29].

2.3.2 Mesh Arrangement

When discretizing the domain, it is necessary to choose the points at which the unknown variable will be computed. As the majority of commercial CFD codes, STAR-CCM+ store all the variables at the same set of grid points and uses the same control volume for all variables. This kind of arrangement takes the name of *collocated*. This approach ensure simplicity to the program especially for complicated domains, but it has some problems with pressure-velocity coupling at the occurrence of pressure oscillations. In the 1980s some special methods were developed (as Rhie-Chow interpolation) that permit to overcome this difficulty and collocated arrangements grids began popular [30].

2.3.3 Discretization Method

Numerical approaches have the particularities to transform a continuous differential equations in algebraic equations, much more handleable for a implementation and solving. With this aim, the equations that govern the motion (1), (4) and (2) are transformed in discrete equations. Regarding the two flow vectorial equations the commercial code STAR-CCM+ solves them in an uncoupled manner although they are clearly bond to each other. The momentum and continuity equations are linked by a predictor-corrector method (SIMPLE). To solve the pressure-velocity incompatibility for collocated variable arrangement, the Rhie-Chow interpolation is used. For more information about discretization methods, see for example [31].

Transient Term

Falling plate is a strongly unsteady problem and time derivative terms have to be discretized. STAR-CCM+ offers two different implicit temporal schemes: first order and second order. The former uses two different time levels, the current time level $(n+1)$ and the previous one (n), while,

in the second order scheme, one more time level appears ($n-1$). In this work, first order scheme was initially used, but, because of the bad accuracy results, second order scheme has been chosen. In addition, this model has the same Δt for each step (fixed time step): in the simulation carried out in this work, Δt can be 2.5×10^{-4} or 5×10^{-4} s depending on the regime considered. The choice depends upon the maximum angular velocity of the plate: to minimize numerical errors, the internal rotating circle can not slide on the external more than one fourth of cell each time step. For tumbling plate, the angular velocity is higher and, besides the smaller dimension of the internal disk, a smaller time steps is necessary.

Convective Term

The convective term is discretized using a second order upwind scheme. The convection face value is calculated by summing at the upstream value a term found by a linear interpolation of the gradients. The Venkatakrishnan limiter is implemented [32]. The scheme is an improvement of the first order upwind, but some numerical diffusion could still exist especially for high gradients.

Diffusive Term

As the previous terms, diffusive term is discretized using a second order scheme. To achieve this objective, it is necessary to introduce a term that takes into account the non-orthogonality of the vector that connect two adjacent cell centres with the control-volume boundary. This is the so called *cross-diffusion* term, and it is treated as a source term when the discretized equations are assembled.

2.3.4 Pressure-Velocity Coupling

As already referred, the continuity and the momentum equations are solved in a uncoupled manner. In order to ensure the correct linkage between pressure and velocity, SIMPLE is used. This algorithm, introduced in 1972 by Patankar and Spalding [33], is basically a predictor-corrector method for the calculation of pressure. In few words, the pressure field is guessed and it permits to calculated the velocity field solving the momentum equations (predictor). However, these velocities do not respect the continuity equation. Through the solving of the pressure correction equation (derived starting from the continuity equation), the velocities will be upgraded (corrector). These steps are solved until the convergence is achieved.

2.3.5 Solving the System of Equation

The discretized equations relative to the single control volume is coupled with the adjacent control volumes. So, in order to obtain the solution, a linear system of equation has to be solved. Due to the large size of the involved matrices, the solution can not be found directly and iterative methods are used. STRAR-CCM+ uses the algebraic multigrid method that consist on the iteration on linear systems of different size (as we had different meshes): this improves a lot the convergence because low-wavelength errors (responsible of a low convergence rate) decrease rapidly on the small matrices whereas short-wavelength errors reduce themselves in the full ones. To solve the three systems of equation (one for each velocity component and

one for pressure) Gauss-Seidel Method relaxation scheme has been used. In addition, for the pressure system of equation, Conjugate-Gradient method as preconditioner is used to improve the convergence rate, while, for the velocities, no preconditioner is necessary because, for its nature, it is usually characterize by a fast convergence rate.

3 VALIDATION STUDY

Measure what can be measured, and make measurable what cannot be measured.

Galileo Galilei (1564-1642)

As every numerical analysis, the results have to be compared with known ones. In this way, the numerical model gains validity and the analysis can proceed. In this chapter the validation study will be conducted. Firstly, it is described the reference model that it has been used to carry out the simulations and afterwards it is shown the final mesh used for this analysis and how it is structured. Finally results are shown and a detailed and critical comparison between literature and numerical results is done.

3.1 REFERENCE MODEL

The tumbling plate studied experimentally by Andersen *et al.* [21] and the same plate investigated numerically by Jin & Xu [26] is taken as reference. It consists on an aluminium plate ($\rho_b = 2700\,\mathrm{kg\,m^{-3}}$) of 0.81 mm of thickness (h) with an aspect ratio $AR = l/h$ of 8 that free falls in water ($\rho_f = 1000\,\mathrm{kg\,m^{-3}}$ and $\nu = 8.8871 \times 10^{-7}\,\mathrm{Pa\,m}$). The value of the acceleration due to gravity is $9.81\,\mathrm{m\,s^{-2}}$. According to [26], the body has an initial inclination of $\vartheta_0 = 45.3^\circ$ with the horizontal axis (counter-clock wise rotations are considered positive) and an initial velocity (parallel to the major plate axes) of $12.615\,\mathrm{cm\,s^{-1}}$.
In this section the aim is to validate our results, therefore, all the previous values are used to perform the simulations.

3.2 MESHES

In order to compute the solution, a mesh convergence study is done. The final and finest mesh (*Mesh 3*) presents five regions with different mesh sizes (see Figure 2). Referring to this figure, the control volumes are smaller and smaller as the colour become darker: this particular arrangement is fundamental to find correctly the fluid motion around the plate and consequently to calculate correctly the fluid forces acting on the body.

The computational domain is discretized with polyhedral cells using the automatic mesh generation of the commercial software used specifying, for each region, the cell base dimension. In addition, to improve the mesh quality, 23 prismatic layers with base size of 2.5×10^{-2} mm (that correspond to grid of 34×260 rectangular control volumes) exist on the surface of the plate (Figure 3 (b)). This kind of mesh is particularly indicated for fluid-body interface because the rectangular cells are aligned with fluid flow. To

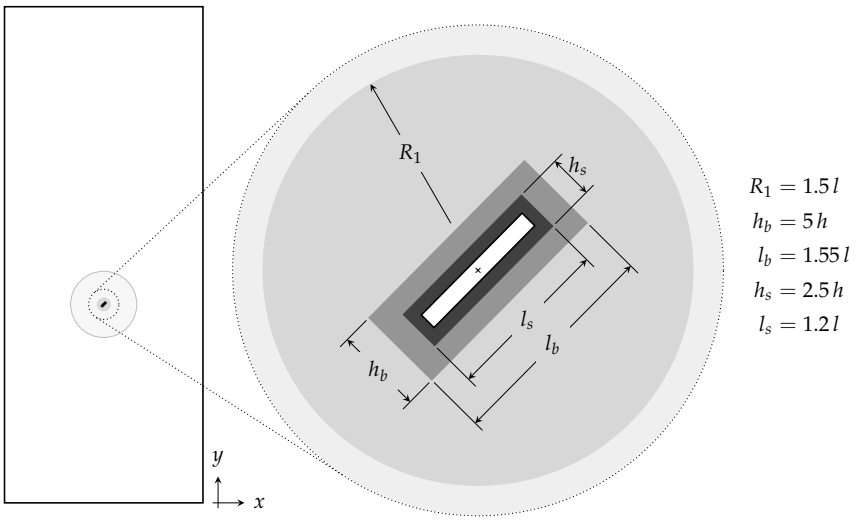

Figure 2.: Mesh refinement regions. Five regions with progressive mesh refinement were defined (one for each colour).

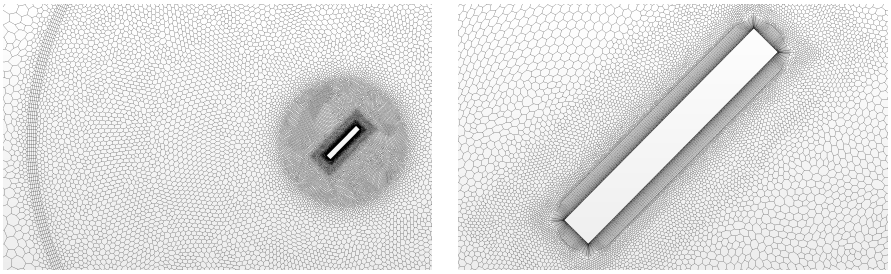

(a) (b)

Figure 3.: Mesh used in the simulation. In (a) we can see the prism layers in the sliding boundary as well as the refinement regions around the plate. In (b) we can see the prism layers that surround the body as well as the different control volumes dimensions.

minimize the interpolation errors, 2 prism layers are also used in each region in correspondence with the sliding boundary (a).
As already referred, in order to simulate a 2D motion, a one-cell-thick three-dimensional mesh is used. To do that, it was necessary to extrude the front surface mesh and delete, in a second time, the old one. The symmetry planes boundary condition ensure that the z velocity component is constantly equal to zero. In these conditions, the computational domain present 60 564 cells, 46 460 of these belong to the rotating region.

3.3 RESULTS

For these simulations a time step of $\Delta t = 2.5 \times 10^{-4}$ s is used. This particular choice is due to the moderately high angular velocity of the tumbling plate: to minimize numerical errors, the internal rotating circle should not slide on the external rectangle more than one fourth of cell each time step.

Table 1.: Comparison between numerical results and literature data (experimental by form Andersen *et al.* [21] and numerical by Jin & Xu [26])

	$\langle v_x \rangle [\mathrm{cm\,s^{-1}}]$	$\langle v_y \rangle [\mathrm{cm\,s^{-1}}]$	$\langle \omega \rangle [\mathrm{rad\,s^{-1}}]$	Descent angle [°]
Experiment [21]	15.9	−11.5	14.5	−35.8
Numerical [26]	15.1	−11.8	15.0	−38.0
Mesh 1	14.0	−7.6	16.9	−28.3
Mesh 2	15.0	−10.5	15.8	−34.9
Mesh 3	15.6	−11.0	15.3	−35.2

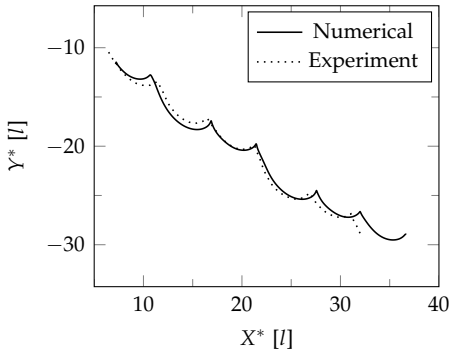

Figure 4.: Trajectories comparison. The numerical results are compared with the experimental ones found by Andersen *et al.* [21]. As we can see, the two trajectories are quite similar.

According to [21, 26], most of results are represented in function of dimensionless parameters. The meaning of these numbers is reported below:

$$U_t = \sqrt{2hg\left(\frac{\rho_b}{\rho_f} - 1\right)} \quad m' = (\rho_b - \rho_f)lh \quad T^* = t\frac{U_t}{l} \quad X^* = \frac{x}{l}$$
$$Y^* = \frac{y}{l} \qquad F_i^* = \frac{F_i}{m'g} \qquad M_i^* = \frac{M_i}{m'gl} \tag{5}$$

where U_t is the average descent speed, obtained by balancing the buoyancy-corrected gravity, $m'g = (\rho_b - \rho_f)hlg$, with the quadratic drag, $\rho_f l U_t^2/2$. The others variables, T^*, X^*, Y^*, F^* and M^* are respectively the dimensionless time, x coordinate, y coordinate, force and torque.

For this analysis three meshes have been used. The average results are showed in Table 1. Here, we can see how, as the mesh becomes finer, the velocities as well as the descent angle increase whereas the angular velocity decreases. The results are in good agreement between those found experimentally by [21]. The numerically study carried out by [26] uses [21] as reference and some bigger discrepancy (if compared with ours) exists for $\langle v_x \rangle$ and the descent angle while $\langle \omega \rangle$ and $\langle v_y \rangle$ prediction are slightly closer to the experiment. In the following will be presented in detailed the results obtained with the finest mesh.

Figure 4 reports the trajectory comparison with the experimental results found by [21]. The pattern find numerically is qualitatively the same and the superimposition is quite good. In any case, in the last part some more discrepancy can be seen: this is expected and it is the error accumulation effect. As we can see the plate falls down with a tumbling motion where centre of mass elevation follows the glide segment. It is important to remark that the trajectories do not start in the origin of the coordinate system. This

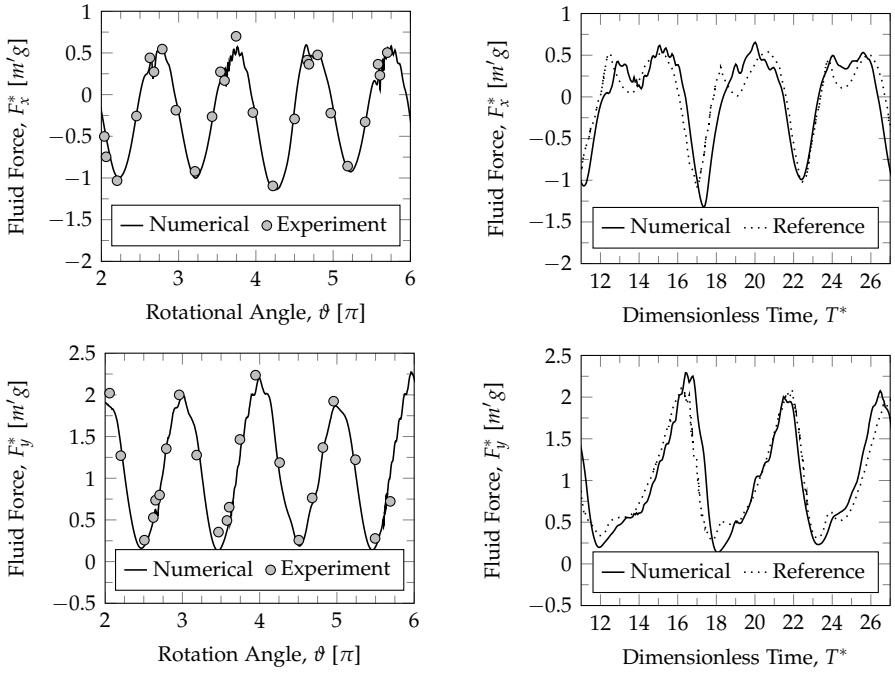

Figure 5.: Fluid force in the x and y directions. The results are compared with the experimental ones found by Andersen *et al.* [21] (plots on the left). On the right side, the numerical work of Jin & Xu [26] is considered as reference.

is due because we are interested in the periodic condition and in the first instants the motion of the plate is not well established.
The next step is to compare the dimensionless fluid forces trend with the one found in literature. In this part both the experimental and numerical results are taken as reference. Figure 5 shows the curve trend of F_x (on the top) and F_y (on the bottom) in function of the plate angle ϑ (on the left) and of the dimensionless time T^* (on the right). Our results fit quite well the experimental points both in the x and in y directions. The model finds correctly the F_x^* minimum values oscillation in correspondence of minimum peaks but some difficulties exist specially for the highest spikes. In the F_y plot there is a little discrepancy in the nearby of $3.5\,\pi$, where a little bit stronger force acts on the Andersen's plate.
Regarding the comparison with the numerical results, the shapes of the curve are similar especially for the F_y. Regarding the hydrodynamic force along the x axes, we notice how the shape is not perfectly the same: our results present a softer valley in correspondence to the pick and in the second period, no value reduction exists. Nevertheless if we try to calculate the dimensionless impulse $\boldsymbol{J}^*$ defined as:

$$J_i^* = \int_{11}^{27} F_i^* \, \mathrm{d}T^* \tag{6}$$

we will find that the difference between our results and those of reference is just -0.524 for F_x^* and 0.298 for F_y^*.
In addition, observing the plots, we can see the presence of a small phase error: it is due to the small angular velocities difference that exist between the two numerical models ($15.0\,\mathrm{rad\,s^{-1}}$ found by the numerical analysis of Jin & Xu against our $15.3\,\mathrm{rad\,s^{-1}}$).

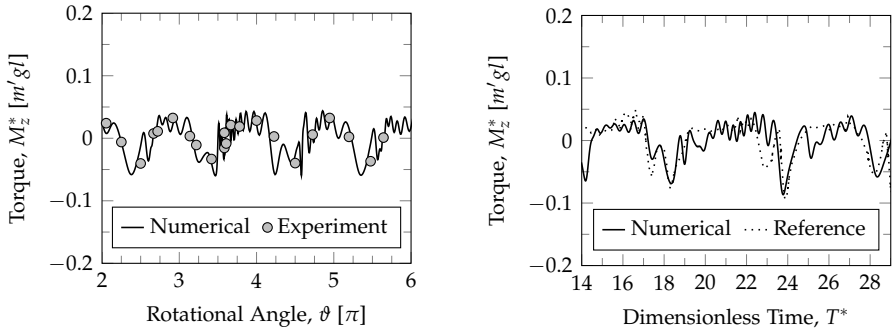

Figure 6.: Fluid torque acting on the body. The results are compared with the experimental ones found by Andersen *et al.* [21] (on the left). On the right side, the numerical work of Jin & Xu [26] is considered as reference.

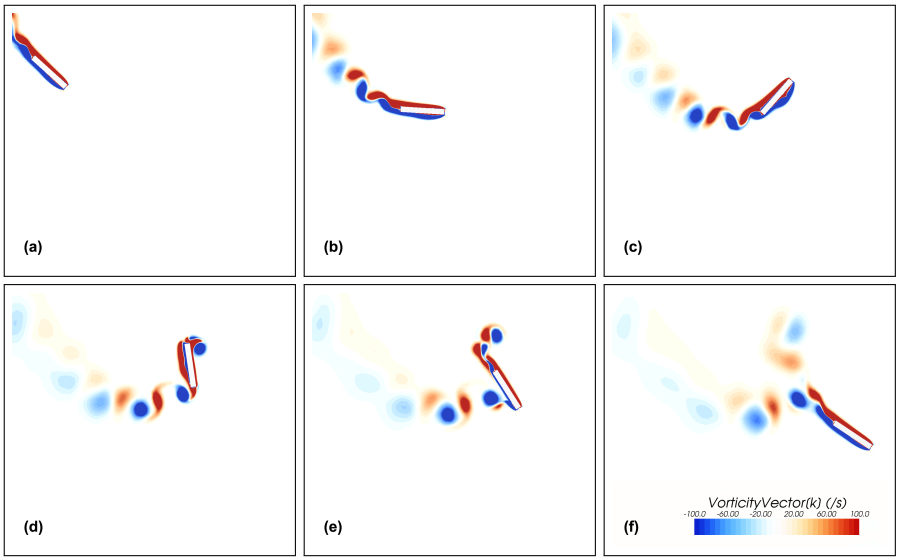

Figure 7.: Vorticity field in at six instant during a full rotation

In Figure 6 it is compared the fluid torque with the results of the same authors. We notice how the torque is characterized by very small values and how it has qualitatively the same trend as the references. In contrast to the previous cases, it has a high frequency oscillation: according to Mittal *et al.* [23] and Jin & Xu [26] this is because the moment is produced principally by the low pressure caused by the vortex shedding phenomena.
In Figure 7 are represented six instants that describe a full rotation of the body. During the fall, the plate glides and gains lift reducing the vertical velocity and, at the same time, the body pitches up due to the fluid torque (a) and (b). The drag increases and consequently the velocities decrease resulting in a cusplike shape near the turning point (d). Note how the wake is always characterized by the shedding of vortices which highly interact with the plate during the rotation at the centre of mass elevations points. In particular in figure (c) we see how the blue vortex that exist on the left side of the body is getting more and more unstable. When the plate decelerates, a new vortex region with the opposite sign (red) is created and the old vortex (blue) sheds on the top of the plate. Afterwards, a new glide starts (e) and the periodic motion is achieved (f).

4 UNCERTAINTY QUANTIFICATION

Somewhere, something incredible is waiting to be known.

Carl Sagan (1934-1996)

This chapter will describe the Non-Intrusive Spectral Projection (NISP) method and the results obtained with this approach. Firstly, a brief introduction is reported in which the choice of this approach is justified. Afterwards, it will be explained which are the uncertain parameters used which is followed by the mathematical formulation of the NISP approach applied to our case. Finally the results obtained with the tumbling and flattering plate will be shown and discussed.

4.1 INTRODUCTION

Both in experiments and in numerical simulation it is important to give an estimation of the errors. In particular, in computational predictions this mean to quantify the confidence intervals of the results for the studied system. As the computers are getting more and more powerful they can handle systems in which the actual physical model can rise high level of complexity and, as consequence, many sources of uncertainties can be introduced. These can be the value of some coefficients like, for example, the combustion rate expression, some thermo-physical proprieties or geometry variable, etc. Most of the times these variables are assumed as ideal or any uncertainties is neglecting, finding, in this way, the so called deterministic solutions.
In this context, the principal aim of stochastic solutions is to find the ensemble average outputs with a confidence interval for a given uncertainty in some input parameters. Nowadays, exist several stochastic approaches, some of each are based on the polynomial chaos decomposition [34]. One of them is the Intrusive Spectral Projection (ISP) that requires a reformulation of the governing equations, considering, from the beginning, the uncertainties on the inputs. In many cases, this kind of approach is not feasible when commercial software with close source code are used. In this field the NISP is a valid alternative approach, in which the stochastic solution is obtained from the results of a series of deterministic solutions [35, 36]. Is this the case of the analysis done in this work where the source code of the commercial software used is not accessible.

4.2 GEOMETRIES

In uncertainty quantification it is necessary to specify which are the stochastic variables and how is the shape of their Probability Density Functions (PDFs) or, at least an extinction of them is required. For this analysis, the uncertainty parameter is the edge of the infinite rectangular body or, equiv-

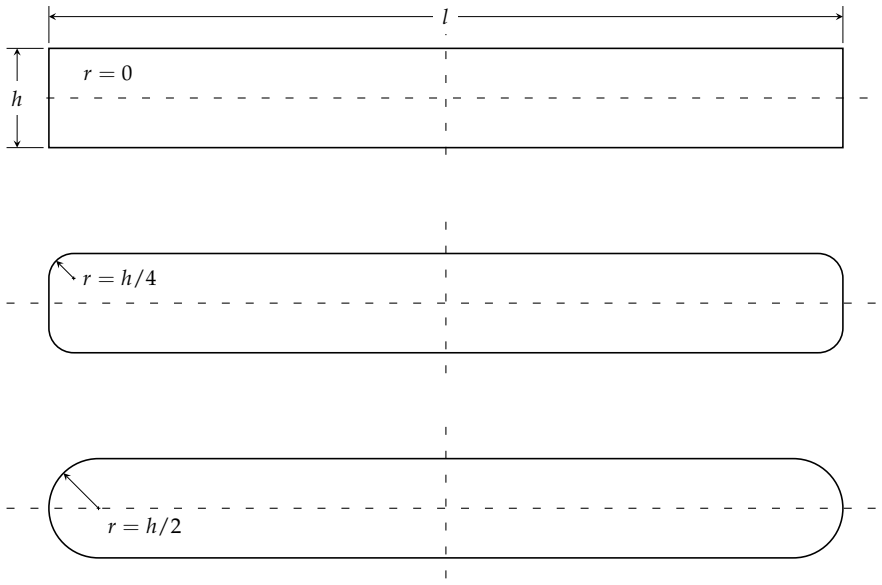

Figure 8.: Representation of the plate with various fillet corners. On the top, the rectangle with $r = 0$ used in the validation, in the middle $r = h/4$ and finally, on the bottom, $r = h/2$. The dashed lines represent the two axis of symmetry of the plate.

alent, the corner of the 2D shape. Precisely, we assumed that all corners are rounded by an arc of circle with a random radius r, sweeping from $r = 0$, corresponding to the rectangular shape, to $r = h/2$, that correspond to a perfectly semi-circular head. In addition, we assume that the four corners have the same radius value, therefore two axis of symmetry exist on the body. Figure 8 represents the two extreme cases and an intermediate one. With these conditions, we have just one stochastic variable, r, that can assume all values inside the interval with the same probability (assumed).

In section 2.2 we remarked how the simulations are not a exactly performed on 2D models because of one-cell-thickness is used. This imply the need to find the second moment of area $\mathcal{J}_z$ and multiplying it by the mesh thickness s and the density of the material in order to find the moment of inertia $\mathcal{I}_{zz}$. The evaluation of $\mathcal{J}_z$ can be done decomposing the body profile in simpler shapes and put everything together using the well-known Huygens-Steiner theorem. In Figure 9 we can see three different geometrical shapes, $\mathcal{S}_1$, $\mathcal{S}_2$ and $\mathcal{S}_3$. The computation of the second moment of area of the two rectangles with respect the z axes passing through $\mathcal{O}$ is trivial:

$$\mathcal{J}_{z1} = \left[h^2 + (l-2r)^2\right] \frac{h(l-2r)}{12} \tag{7}$$

$$\mathcal{J}_{z2} = \left\{\left[r^2 + (h-2r)^2\right] \frac{1}{12} + \left(\frac{l}{2} + \frac{r}{2}\right)^2\right\} r(h-2r) \tag{8}$$

Let us consider a quarter of circle. It is known that the second moment of area passing through the corner is $\pi r^4/8$. For applying the Huygens-Steiner theorem, $\mathcal{J}$ has to be calculated with respect the axes passing through the centroid of area situated at $4r/(3\pi)$ far (both in x and in y directions) from

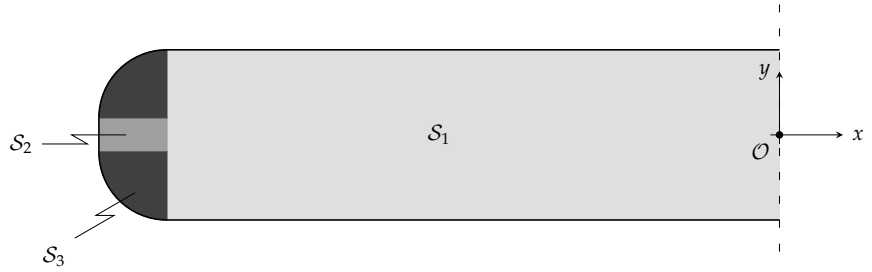

Figure 9.: Decomposition of the body profile in several regions ($\mathcal{S}_1$, $\mathcal{S}_2$ and $\mathcal{S}_3$). In the figure it is also represented the barycentre $\mathcal{O}$ of the body and the referential frame used.

the corner. Now it is possible to compute $\mathcal{J}_{z3}$ with respect the $\mathcal{O}$ point. We have:

$$\mathcal{J}_{z3} = \left[\frac{r^2}{8} \underbrace{-\left(\sqrt{2}\frac{4r}{3\pi}\right)^2}_{\text{translation to the centroid}} \underbrace{+\left(\frac{l}{2} - r + \frac{4r}{3\pi}\right)^2 + \left(\frac{h}{2} - r + \frac{4r}{3\pi}\right)^2}_{\text{translation to the } \mathcal{O} \text{ point}}\right] \frac{\pi r^2}{4} \tag{9}$$

Finally, considering the total number of regions, we have:

$$\mathcal{J}_z = \mathcal{J}_{z1} + 2\mathcal{J}_{z2} + 4\mathcal{J}_{z3} \tag{10}$$

As we can see, the moment of inertia is a function of r and it decreases as the fillet radius increases. The relative difference between the two extreme values is 7.74%, too big to be neglected. So, in the further simulations, the real mass and moment of inertia are considered and no approximations are done.

4.3 MATHEMATICAL FORMULATION

As already mentioned, NISP method uses deterministic results in order to calculate the stochastic solution. The specific mathematical model applied to this analysis will be described here.
Let us consider r as the uncertainty parameter of the model that it is associated with the random variable ξ. Using a Polynomial Chaos expansion, is possible to express r in function of ξ:

$$r(\xi) = \sum_{n=0}^{q} \hat{r}_n \varphi_n(\xi) \tag{11}$$

where $\hat{r}_n$ are the expansion mode coefficients and φ_n are orthogonal polynomials of order n. From the previous formula, we can remark that the first term, $\hat{r}_0$ is the mean, $\hat{r}_1$ is the coefficient of the linear term, $\hat{r}_2$ the one of the quadratic term and so on. According to [37], depending on the PDF of r, exists an optimal set of orthogonal polynomials φ_n associated with the random variable ξ that minimizes the required number of terms in the previous expansion. In this analysis, we considered a uniform distribution for

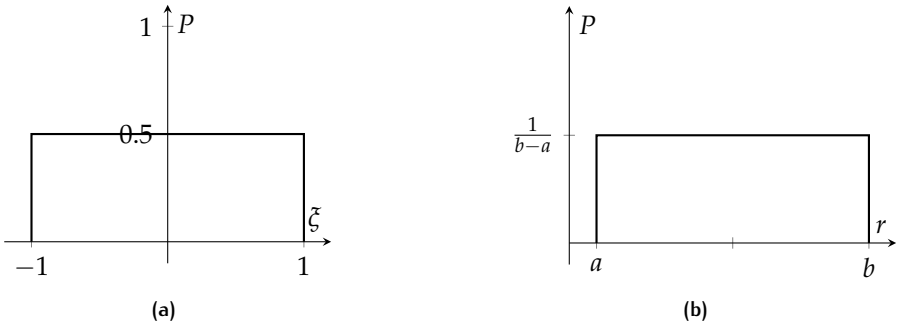

Figure 10.: The uncertainty was supposed to have a uniform distribution. In (a) is represented the case used for the calculation of the stochastic model while in (b) the variable in the geometrical model r is shown.

r, therefore, the optimal set of orthogonal polynomials in (11) is given by the Legendre polynomials, defined by:

$$\begin{cases} \varphi_0(\xi) = 1 \\ \varphi_1(\xi) = x \\ \dots \\ \varphi_n(\xi) = \dfrac{(2n-1)}{n}\xi\varphi_{n-1}(\xi) - \dfrac{(n-1)}{n}\varphi_{n-2}(\xi) \\ \varphi_{n+1}(\xi) = \dfrac{(2n+1)}{n+1}\xi\varphi_{n-1}(\xi) - \dfrac{(n)}{n+1}\varphi_{n-1}(\xi) \end{cases} \tag{12}$$

In the previous definition, the random variable ξ as a uniform distribution with zero mean and $1/\sqrt{3}$ standard deviation (Figure 10 **(a)**. In **(b)** it is represented the general case of the uniform distribution. Following the definition of equations (11) and (12) and considering Figure 10 we have:

$$r(\xi) = \frac{a+b}{2} + \frac{b-a}{2}\xi \tag{13}$$

Considering the Legendre polynomials, they have an important propriety which is the bedrock of the present formulation. They have the peculiarity to be orthogonal to each other with respect to the inner product in the interval $[-1, 1]$:

$$\left\langle \varphi_i, \varphi_j \right\rangle = \int_{-1}^{1} \varphi_i \varphi_j W(\xi)\, \mathrm{d}\xi = \frac{1}{2j+1}\delta_{ij} \tag{14}$$

where δ_{ij} is the Kronecker delta function and $W(\xi)$ is the weighting function for the probabilistic case which is equal to $1/2$.

Let us introduce a new variable, the solution of the system, f which, for the previous considerations, is function of ξ, $f(\xi)$. We can express it by using the Polynomials Chaos expansion (11) leading to:

$$f(\xi) = \sum_{j=0}^{Q} \hat{f}_j \varphi_j(\xi) \tag{15}$$

where $\hat{f}_j$ are the unknown expansion mode coefficients and, because of just one uncertainty variable is consider (mono-dimensional case), the total Q is equal to the highest Legendre polynomial considered.

If we multiply both sides of equation (15) by φ_k and calculate the inner product (14) we have:

$$f\varphi_k = \left(\sum_{j=0}^{Q} \hat{f}_j \varphi_j\right) \varphi_k \quad \longrightarrow \quad \int_{-1}^{1} f\varphi_k \, \mathrm{d}\xi = \sum_{j=0}^{Q} \hat{f}_j \int_{-1}^{1} \varphi_j \varphi_k \, \mathrm{d}\xi \quad \longrightarrow$$

$$\int_{-1}^{1} f\varphi_k \, \mathrm{d}\xi = \hat{f}_k \frac{1}{2k+1}$$

hence

$$\hat{f}_k = \int_{-1}^{1} f\varphi_k \, \mathrm{d}\xi \, (2k+1) \tag{16}$$

The previous integral will be estimated using the Gauss-Legendre quadrature:

$$\int_{-1}^{1} f\varphi_k \, \mathrm{d}\xi \approx \sum_{i=1}^{N_p} f(\xi_i) \, w_i \, \varphi_k(\xi_i) \tag{17}$$

where ξ_i are the considered points which are found imposing the highest polynomials φ_{N_p} equal to zero. The weights, w_i, are calculated by the formula (see [38]):

$$w_i = \frac{2}{(1-\xi_i^2)\left(\varphi'_Q(\xi_i)\right]^2} \tag{18}$$

and $f(\xi_i)$ are the deterministic solutions found carrying out the simulations with the commercial software. Note how, if a Legendre polynomial of grade N_p is considered for finding the ξ_i, the integral solution is approximated with a $N_p - 1$ polynomial grade ($\varphi_{N_p}(\xi_i)$ will vanish in correspondence of the considered nodes). Once the expansion coefficients $\hat{f}_k$ are known we can find the solution $f(\xi)$ from equation (15) and the correspondent PDF which, in this analysis, it has been constructed using the kernel density estimation method [39].

4.4 RESULTS

In this section will be described and discussed the obtained results. At first the uncertainty analysis is applied to the tumbling plate and then the study is extended to the fluttering case.
The objective is the same for the two different regimes. We are interested in plotting the average trajectory and in giving an estimation of the results when a confidence interval of 95% is considered. In addition, we are looking for the PDF that describes the X^* solution when a specified Y^* is imposed, or in other words, the horizontal position after a fall of specified height.

4.4.1 Tumbling Plate

In order to conduct the uncertainty analysis, the tumbling plate described in section 3 is used as well as the same mesh parameters (minimum cell values, refinement regions, etc.). We are interested in finding the deterministic solution $f(\xi_i)$ to perform the integral 17 using the Gauss-Legendre quadrature.

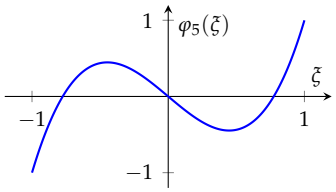

Figure 11.: Third order Legendre polynomial.

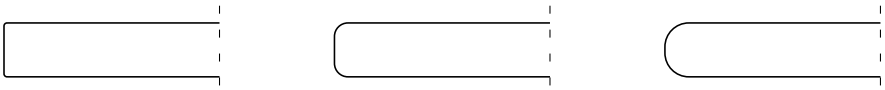

Figure 12.: The three plates used for the stochastic plot are represented here. On the left we find r_1 to which follow the plates with radius r_2 and r_3.

Three points approximation

At first we suppose that the solution function $f(\xi)$ is approximated with a quadratic polynomial, *i.e.* we have to consider $\varphi_3(\xi)$ as polynomial with the maximum grade. If we will reach the convergence, the process will stop and results are considered valid, if not, it is necessary to increase the number of integration points, choosing a higher order Legendre polynomials for finding the new roots ξ_i. Following the definition of equation (12) the polynomial $\varphi_3(\xi)$ is (the plot of the function in reported in Figure 11):

$$\varphi_3(\xi) = \frac{1}{2}(5\xi^3 - 3\xi) \tag{19}$$

which has solution for $\varphi_3(\xi) = 0$

$$\frac{1}{2}\xi(5\xi^2 - 3) = 0 \qquad \longrightarrow \qquad \begin{cases} \xi_1 = -\sqrt{3/5} \\ \xi_2 = 0 \\ \xi_3 = \sqrt{3/5} \end{cases} \tag{20}$$

and the corresponding weights are given by (18):

$$w_{1,3} = \frac{5}{9} \qquad\qquad w_2 = \frac{8}{9} \tag{21}$$

The numerical simulations are therefore carried out in the points given by equation (13) when $a = 0$ and $b = h/2 = 0.81\,\text{mm}$ finding:

$$\begin{cases} r_1 = 0.0456\,\text{mm} \\ r_2 = 0.2025\,\text{mm} \\ r_3 = 0.3595\,\text{mm} \end{cases} \qquad \text{or in terms of } h/2 \qquad \begin{cases} r_1 = 11.27\% \\ r_2 = 50.00\% \\ r_3 = 88.73\% \end{cases} \tag{22}$$

The three different plate shapes can be seen in Figure 12. The simulations were performed for a physical time of 5 s which correspond, in our condition, to a dimensionless time of 126.8 (see (5)). Results are reported in Figure 13. As we can see, as the radius increases, the trajectories become more and more horizontal and the glides get smaller and smaller. This is as expected because the edges are less sharp and, as consequence, less separation exists: the plate gains not only more lift but also it acts in a more constant manner which permit to have a smoother and less inclined trajectory. Vortex shedding process still exists but it is not so accentuate as we

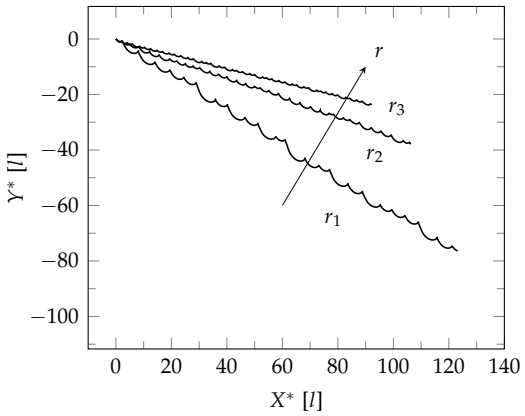

Figure 13.: Trajectories for the tumbling plate when three different radii are considered. Note how the falling angle decreases as the corners become less sharp.

Table 2.: Comparison between the three different plates with different fillet radius.

	$\langle v_x \rangle [\mathrm{cm\,s^{-1}}]$	$\langle v_y \rangle [\mathrm{cm\,s^{-1}}]$	$\langle \omega \rangle [\mathrm{rad\,s^{-1}}]$	Descent angle [°]
r_1	15.2	−9.4	15.8	−31.7
r_2	13.8	−4.9	20.7	−19.6
r_3	12.1	−3.1	26.3	−14.4

can see in Figure 14. In Table 2 are reported the mean values of the three runs. As the radius become bigger, both the velocity along the x and y axis decrease while, the average angular velocity increases. The results are completely in accordance with those found during the code validation and reported in Table 1: as we can verify, the trend of all variable is respected.

Until now we have just described the deterministic results and no stochastic analysis has been done. Let us start now with the uncertainty analysis. As already referred our objective is to plot the ensemble average trajectory for confidential interval of 95%. If we find the expansion coefficients $\hat{f}_k$ for both the solution in x and y axis for a given time (as describe in the previous section), we will find the stochastic solution and we will be able to plot the PDFs: from these it is possible to find the ensemble average and the confidential interval wanted. Computing them for all time step, we can find the plot reported on the left side of Figure 15. As we can observe, the X^* coordinate is almost a linear function of r and the median, which separates the higher half probability distribution from the lower half, is quite exactly at the middle of the two boundaries that describe the uncertainty range. On the right are reported the coefficients of the solution calculated in three different instant, $T^* = 40$, $T^* = 80$ and $T^* = 120$. In this bar plot, the coefficients are getting smaller and smaller as the polynomial grade increases – see 15 – almost vanish for the second order. This is a good indicator about the convergence.

Let us analyse the behaviour of the Y^* coordinate, Figure 16. The meaning of the plot is the same as beforehand. Now, the plot on the left reveals how the trend is not linear: a small variation or the fillet radius in the low range has a much more influence of the same variation for big r. Regarding the bar diagram, we see how the coefficients are getting smaller as the polynomial grade increases, but, since $\hat{f}_3$ can not be neglected and considered as zero, we conclude that the convergence is not reached for the Y^* coordinate. We

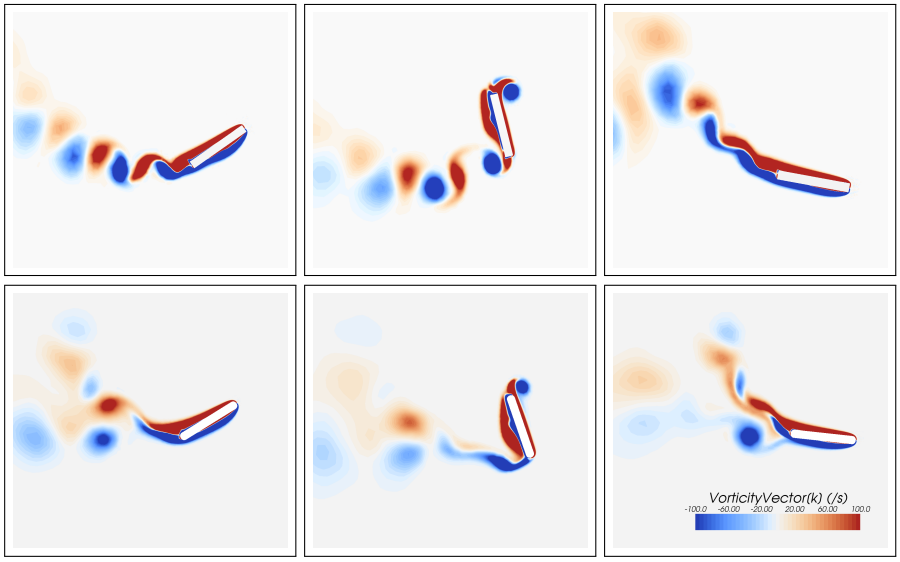

Figure 14.: Vorticity field around the plates with fillet radius r_1 (top) and r_3 (bottom). As we expected the wake is different and vortex shedding is much more intensive for sharper corners.

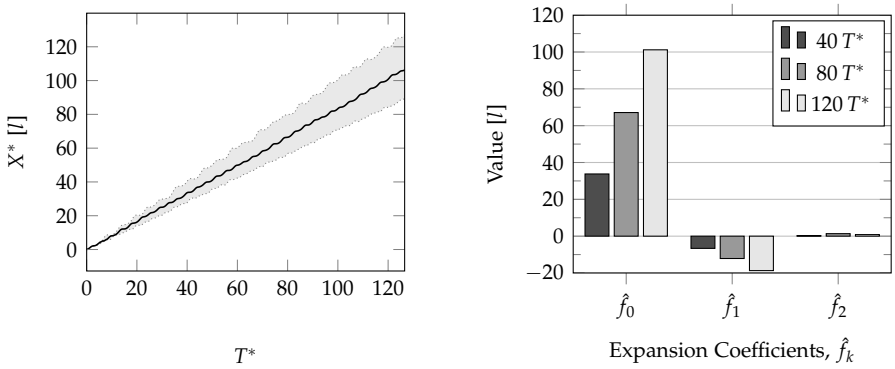

Figure 15.: X^* position in function of the time. The grey area represents the uncertainty at which the plate is subjected while the black line plots the stochastic PDF median. On the right, the solution coefficients at three different instants.

need to increase the number of points in order to increases the grade of polynomial that approximate the solution.

Five points approximation

We have seen how approximating the Y^* solution by the quadratic approximation the convergence was not reached. In this part we will perform the previous steps, but conducting the Gauss-Legendre quadrature using five points. They are given by the roots of the fifth order Legendre polynomial (see Figure 17):

$$\varphi_5(\xi) = 0 \qquad \longrightarrow \qquad \frac{1}{8}\xi(63\xi^4 - 70\xi^2 + 15) = 0 \tag{23}$$

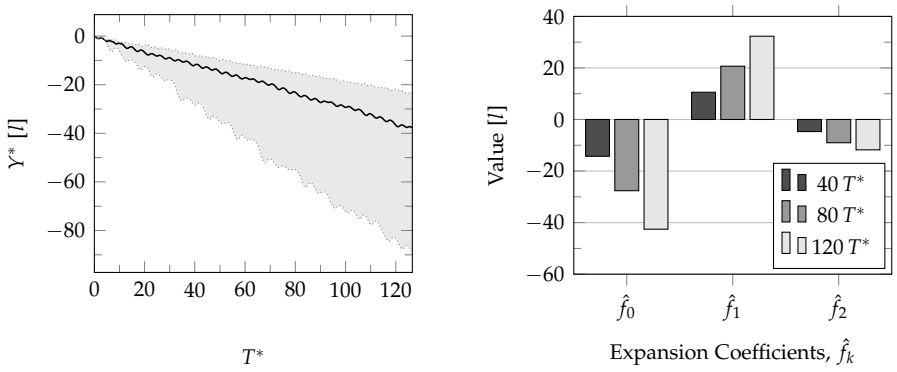

Figure 16.: Y^* position in function of the time. The grey area represents the uncertainty at which the plate is subjected while the black line plots the PDF median. On the right, the solution coefficients at three different instants. As we can see, the convergence is not reached.

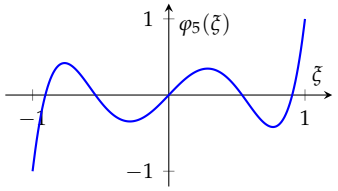

Figure 17.: Fifth order Legendre polynomial.

which, after the coordinate transformation, become:

$$\begin{cases} r_1 = 0.0190\,\text{mm} \\ r_2 = 0.0935\,\text{mm} \\ r_3 = 0.2025\,\text{mm} \\ r_4 = 0.3115\,\text{mm} \\ r_5 = 0.3860\,\text{mm} \end{cases} \quad \text{or in terms of } h/2 \quad \begin{cases} r_1 = 4.69\% \\ r_2 = 23.08\% \\ r_3 = 50.00\% \\ r_4 = 76.92\% \\ r_5 = 95.31\% \end{cases} \tag{24}$$

Performing the simulations, we found the results shown in Figure 18 while, in Table 3, are summarized the average values. As we expected the trajectories form with the horizontal an angle that is, in absolute value, smaller and smaller. Note how they are perfectly in accordance with both Table 2 (three points) and Table 1, which summarize the mesh convergence results. In addition we see how the trajectories do not sweep equally in space, but a concentration of the path for low and high fillet radius value seems happen: for instance the path drawn by r_2 is much closer to that of r_1 and the same behaviour appears for high value of r. We could immediately conclude without any stochastic calculations that the resulting PDF will not be constant, but it will be a kind of bimodal distribution.

We can now proceed with the stochastic analysis. The procedure is exactly the same as the three points case: initially, we look for the convergence of the solution in function of the time and only afterwards the stochastic solution resulting on a fall of a certain height will be calculated.
Figure 19 shows the stochastic solution in function of the time and the grey area represents, as beforehand, the uncertainty (with 95% confidence interval) of the X^* value. It is interesting to note that the uncertainty growths almost linearly with the time: that is a directly consequence of plot Figure 18 in which the trajectories diverge one of each other. In correspondence of

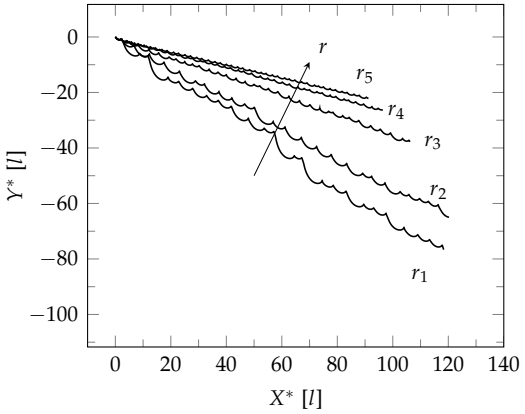

Figure 18.: Trajectories for the tumbling plate when five different radii are considered. As beforehand, the falling angle decreases as the corners become less sharp.

Table 3.: Comparison between the five different plates with different fillet radius.

	$\langle v_x \rangle [\mathrm{cm\,s^{-1}}]$	$\langle v_y \rangle [\mathrm{cm\,s^{-1}}]$	$\langle \omega \rangle [\mathrm{rad\,s^{-1}}]$	Descent angle [°]
r_1	15.2	−9.4	15.8	−31.7
r_2	15.0	−8.4	16.0	−29.2
r_3	13.8	−4.9	20.7	−19.6
r_4	12.5	−3.4	25.1	−15.2
r_5	12.0	−3.0	26.9	−14.0

$T^* = 40$, $T^* = 80$ and $T^* = 120$, are drawn three PDFs of the solution at that instant. As we expected, they are characterized by a peak at each interval extremity: it is quite strong for low time values getting smoother and smoother as the time goes by until almost become constant for high fillet radius value (in the plot high radius are below to the median line). On a bar diagram the five coefficients of the solutions calculated in that intervals are plotted. We can see how the stochastic mean, $\hat{f}_0$ is the main term and the coefficient of the linear polynomial, $\hat{f}_1$, plays an important role. The two-peaks shape, bimodal distribution, seems to be given by the joint action of cubic and linear term contributions while the second and fourth order polynomials do not seem to enter in the polynomial chaos expansion. Since the higher order coefficients are quite small, we can assume that the convergence is reached and therefore further improvements would not modify significantly the PDFs shape.

Regarding the Y^* variable, the results obtained with the five points approximation are shown in Figure 20. The PDFs shape are equal to X^* solution, becoming almost constant for high time values. We can see how, in this case, the uncertainties are much bigger than the previous one. In correspondence of $T = 120$, the uncertainties enclose an interval of more then $60\,l$ in contrast with $35\,l$ of the X^* solution.
The bar diagram shows how the modulus of the five solution coefficients is getting smaller and smaller as the polynomial grade increases. As beforehand, we can assume that the convergence is reached since the $\hat{f}_4$ coefficients are all smaller than 5% of $\hat{f}_0$.

As briefly wrote in the beginning of this section, one of the objectives of this study is to find the PDF that describes the X^* solution when a prescribed fall is imposed. In the further analysis one fall of $Y^* = -17.5\,l$ and an other of $Y^* = -35\,l$ are considered. From Figure 18 it is possible to

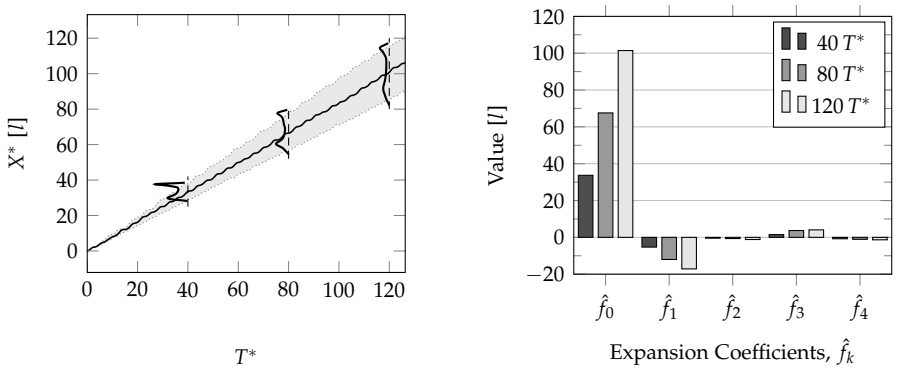

Figure 19.: X^* position in function of the time. The grey area represents the uncertainty with a 95% confidential interval at which the plate is subjected while the black line plots the PDF median. In addition, PDF are represented at three different instant. Note how in the shape exist two peaks which are getting smoother and smoother as the time increases. On the right, are shown the five coefficients of the solution found in the three different instants.

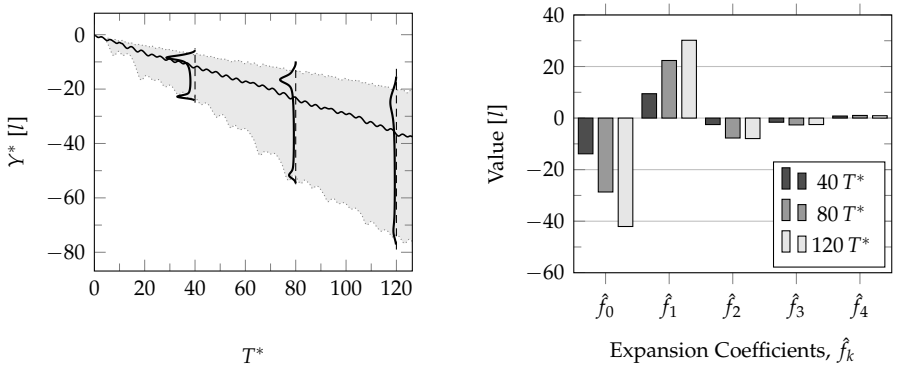

Figure 20.: Y^* position in function of the time. The grey area represents the uncertainty at which the plate is subjected while the black line plots the median of PDF. In addition, PDFs are represented at three different instant. Note how in the shape exist two peaks which are getting smoother and smoother as the time increases. On the right, are shown the five coefficients of the solution found in the three different instants.

note how the r_4 and r_5 plate do not reach the lower Y^* coordinate so, an extension of the physical time until 7 s ($T^* = 177.6$) and 8 s ($T^* = 202.9$) respectively was needed. Figure 21 reports the extended trajectories as well as the reference levels that will be considered for the stochastic calculations.

Figure 22 shows the results for the two different falls. On the top, is reported the PDF for the small fall, *i.e.* after a vertical distance of $17.5\,l$ while on the bottom there is the solution for $Y^* = -35\,l$. The two PDFs are quite similar, both are a kind of bimodal distribution. The particular shape is in accordance with the deterministic solutions, reported in the same plot with black points: at the extremities they are closer to each others, causing in this way a probability increase. Besides the PDFs, the plots reports the confidential interval of 95%, represented with the shadowed areas. On the right, as usually, the expansion coefficients are plotted in a bar diagram showing how the importance of the high order polynomials is getting less and

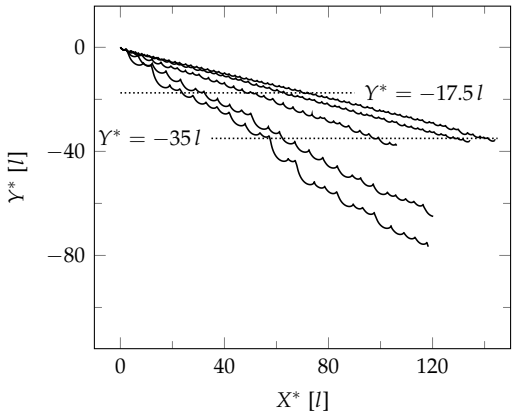

Figure 21.: In this picture are reported the extended trajectories. In addition, with dotted lines, are represented the considered reference levels.

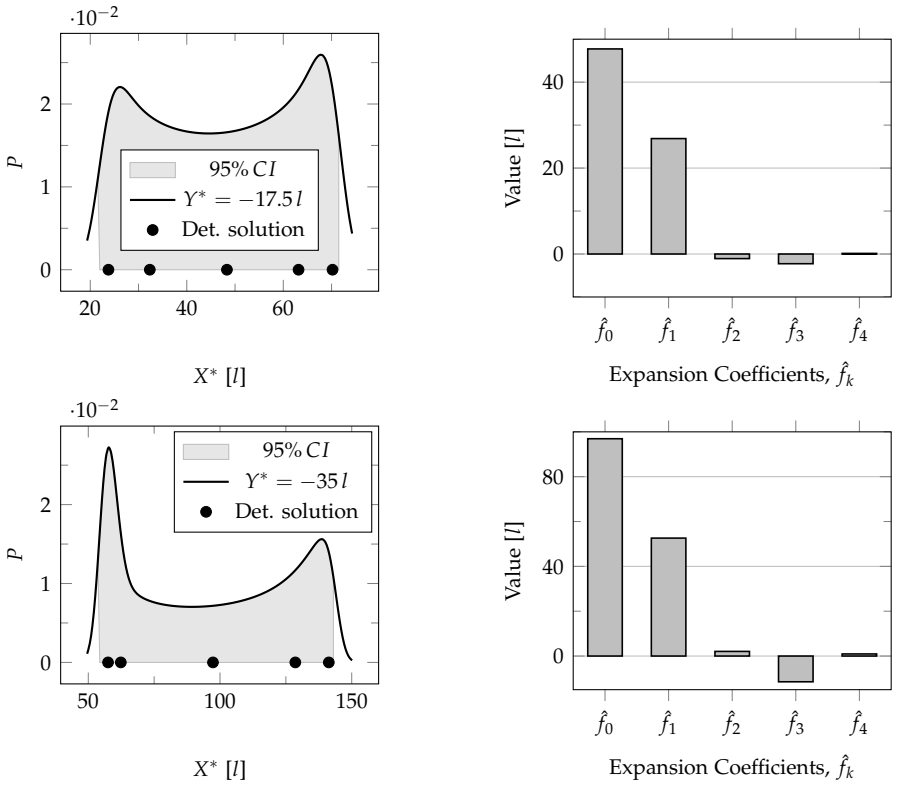

Figure 22.: X^* position after a fall of $17.5l$ (top) and $35l$ (bottom). On the left, the PDFs trend and the respective confidence intervals (grey areas). Deterministic solutions (see Figure 21) are also plotted. On the right, we find the various expansion coefficients.

less important and almost vanished in correspondence to the fourth order. Hence, we supposed that the convergence is reached and we can conclude that the system do not follows a linear law, but a concentration of events exist in correspondence of the interval extremities (bimodal distribution).

4.4.2 Fluttering Plate

Until now, we have considered the plate falls down with the tumbling motion *i.e.* it spins and translates at the same time and the trajectory can be approximated with a straight line inclined by a certain angle. However, this is not the unique possible motion because, depending upon the dimensionless coefficients (see section 2.1), fluttering can occur. According to [21], fluttering appears when the length of the plate l is increased in such a way the aspect ratio AR is equal to 14. All the other dimensional parameters are kept constant.
For the simulations, the same mesh parameters as beforehand are considered but, to take account of the new dimensions, the computational domain will be enlarged following the relations of Figure 2. Regarding the time step interval, in 3.3 was written that in order to minimize numerical errors, the internal rotating circle can not slide on the external domain more than one fourth of cell each time step. In this case, in contrast with the previous, the body angular velocity is lower and, although the dimensions are bigger and therefore the sliding velocity is amplified, a fixed time step of $\Delta t = 5 \times 10^{-4}$ s can be used.

Five points approximation

As the tumbling case, the objectives are the same, that are find the ensemble average trajectory, the median value, the associated confidential interval and the plate position after a fall of a specified height.
Considering directly five points, *i.e.* the same as (24), we find the trajectories reported in Figure 23 (a).
Before analysing the results through a stochastic point of view and conducting the convergence study, we notice that the centre of mass elevation points, after the first glide, appear sequentially and in an almost linear manner as the fillet radius increases. However, after the second glide, the path relative to the plate with fillet radius r_4 stays between the r_1 and r_2 trajectories and not, as we would have expected, between r_3 and r_5 (see zoom in Figure 23 (b)). For understanding this behaviour, the interval between r_3 and r_4 was subdivided in four equally spaced parts, calling the nodes in between r_{334}, r_{34} and r_{344} while in the interval $[r_4, r_5]$ was introduced just one point in the middle, r_{45} (see Figure 24). Simulations were performed with these new values of fillet radius and the results confirm the anomaly highlighting how the locus of the peaks points initially increases its ordinate value in an almost linear manner. Afterwards, the curve inverts the trend going backwards and reaching its minimum X^* value with r_{344} before taking one more time the right direction and, after r_4, an apparently linear behaviour appears. The previous considerations can be well appreciate in Figure 23 (c): a black line helps to follows the various peaks.

In order to find the physical explication of this behaviour, the vorticity field around the plates was observed. We took as reference models, the plates with fillet radius equal to r_3, r_{344} and r_{45}. To complete the study, three different time instants are considered: the first, t_1 is when the plate

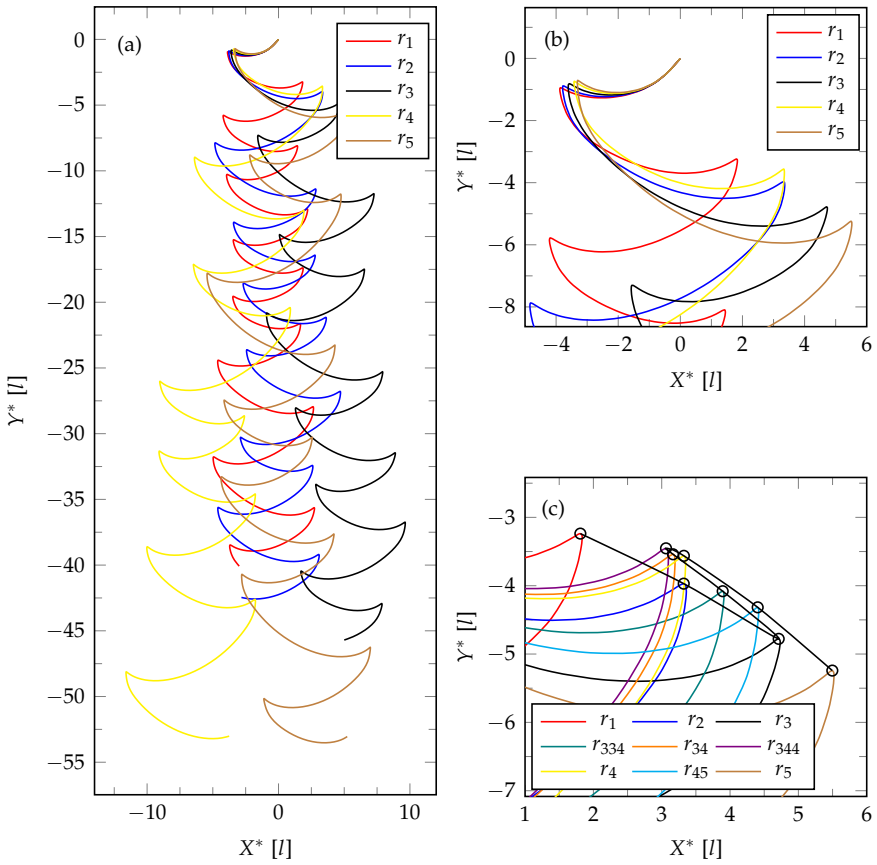

Figure 23.: Plot (a) shows the five trajectories corresponding to the Gauss-Legendre fillet radius points. In (b) a particular of the first two glides are represented. Note the anomaly of the trajectory drawn by the r_4 plate. In (c) we find the deterministic solution for intermediate cases. The black line marks the locus of peaks points.

stays in the horizontal position, *i.e.* the local and the global reference frames are superimposed; in the second instant, t_2, the plate is at the maximum centre of mass elevation point and, the third one t_3 is considered equal to $t_3 = t_2 + (t_2 - t_1)$. Results are shown in Figure 25. Observing the pictures we notice how the interaction between vortexes and body exists especially when the body starts to descends. Let us analyse the images placed in the first row: the vorticity field appear very similar, but small differences in the wake structure can be appreciate between the three picture. Regarding the second row, these differences become more accentuate and the vorticity field assume an other pattern: the r_3 plate has the vortex which is shedding on the upper part of the trailing edge, in the centre plates it is on the lower side and in that placed on the right the shed on the lower side is just conclude. Since the vorticity is directly bound with the velocities field, it means that the pressure field is different, therefore the forces acting on the body will have some variations.
Resuming, we can conclude that since the geometry of the body is slightly different, will also be the vorticity field around the plate. As the time goes

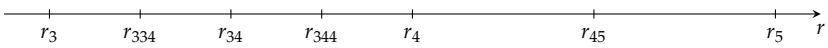

Figure 24.: In order to investigate the anomaly of the trajectories, the interval between r_3 and r_4 is divided in four equal intervals while the one between r_4 and r_5 has just one point in the middle, r_{45}.

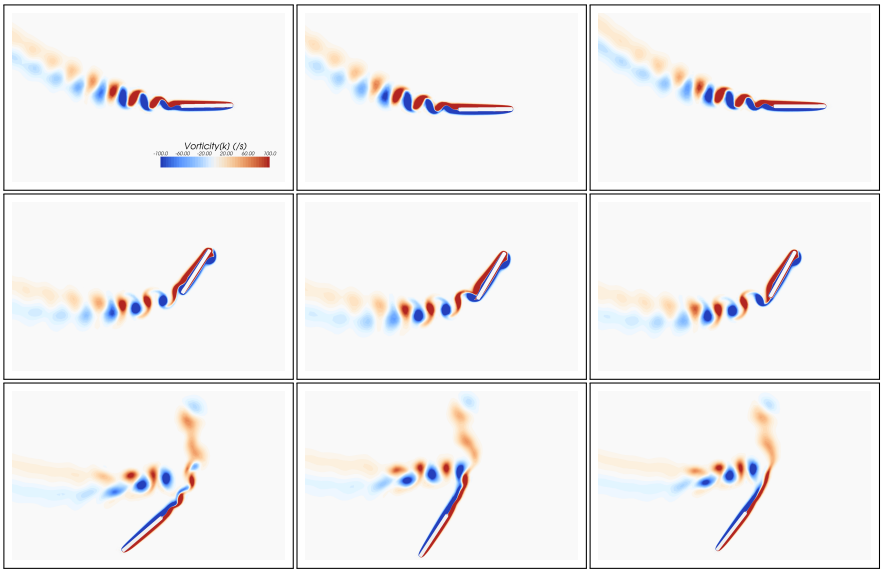

Figure 25.: Vorticity field around the fluttering plate. (a), (b) and (c) are respectively the solution of r_3, r_{344} and r_{45}. From this picture we can see how the vortex shedding process interacts with the body.

by, these small differences are amplified causing a macroscopic phenomena, that is, in our case, the behaviour of the locus of the peaks points.

Coming back to the stochastic analysis, five deterministic solutions are few to ensure convergence. For instance, we tried to plot the PDFs at some specified time, but we found that the coefficients of high order polynomials were much higher than the one which describes the stochastic average, $\hat{f}_0$. A similar behaviour means that we are far from the convergence, therefore, we opted to increase the number of points to nine without experimenting the seven points approximation.

Nine points approximation

In order to find the nine points, the roots of the following Legendre polynomial were found (see Figure 26):

$$\varphi_9(\xi) = \frac{\xi}{128}(12155\xi^8 - 25740\xi^6 + 18018\xi^4 - 4620\xi^2 + 315) = 0 \qquad (25)$$

it gives nine solutions that after the coordinate transformation become:

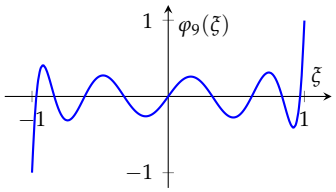

Figure 26.: Ninth order Legendre polynomial.

$$\begin{cases} r_1 = 6.447 \times 10^{-3}\,\text{mm} \\ r_2 = 3.320 \times 10^{-2}\,\text{mm} \\ r_3 = 7.829 \times 10^{-2}\,\text{mm} \\ r_4 = 0.1368\,\text{mm} \\ r_5 = 0.2025\,\text{mm} \\ r_6 = 0.2628\,\text{mm} \\ r_7 = 0.3267\,\text{mm} \\ r_8 = 0.3718\,\text{mm} \\ r_9 = 0.3986\,\text{mm} \end{cases} \quad \text{or in terms of } h/2 \quad \begin{cases} r_1 = 1.59\% \\ r_2 = 8.20\% \\ r_3 = 19.33\% \\ r_4 = 33.79\% \\ r_5 = 50.00\% \\ r_6 = 66.21\% \\ r_7 = 80.67\% \\ r_8 = 91.80\% \\ r_9 = 98.41\% \end{cases} \tag{26}$$

As the case with five points, nine deterministic solutions are not sufficient to guarantee the convergence because, as the polynomial grade increases, the coefficients become higher and higher. As consequence, we would need much more points for properly analysing the flattering plate. An alternative is to restrict the interval of the radius random variable r.
The initial interval $[0, h/2]$ was subdivide in four equal parts and the analysis was performed with 9 points in $[0.75\frac{h}{2}, \frac{h}{2}]$ to avoid the interval in which peaks inversion phenomena occurs. The number of sample suggests that 36 points are not enough to ensure convergence and a very large number of samples (hundreds) is required. This is due to a small perturbation in the input variable, causes a large variability of the trajectory path requiring a large number of degree of freedom to stochastically analyse the problem.
The computing time for 155×10^3 control volumes and 10^4 time steps is around 75 CPU hours for each unsteady deterministic calculation, consequently the problem can only be treated with high performing computing. Previous investigation [21, 24, 25] have reported that the regimes of 2D free fall plate can be tumbling, fluttering, steady fall and chaotic regime with a mixture of tumbling and fluttering. The present case of perturbation of the fluttering regime undergoes a chaotic path trajectory preserving the fluttering motion.

In order to understand the importance of the vortex shedding in the fluttering regimes, three plates were considered at rest and simulations were carried out. The bodies are aligned with the flow that has a velocity magnitude of $0.35\,\text{m}\,\text{s}^{-1}$, that is a typical velocity in the fluttering regime. In this case the Reynold's number is equal to $\text{Re} = 4466$ while, during the fall, it can vary between 200 and 5800. The considered plates present a fillet radius relatively to $\frac{h}{2}$ of $r_1 = 1.59\%$ (see (26), chosen to avoid the 90 degree corner), $r_2 = 50\%$ and $r_3 = 100\%$. Figure 27 shows that as the corners become less sharp, the force amplitude decreases while the frequency increases following a non-linear law. The forces developed by the sheds of the vortices represent a percentage that can reach up to 23% of the total fluid force for small fillet radius while the value reduces to 10% for a completely round head. For higher velocities, the phenomena become stronger and both the

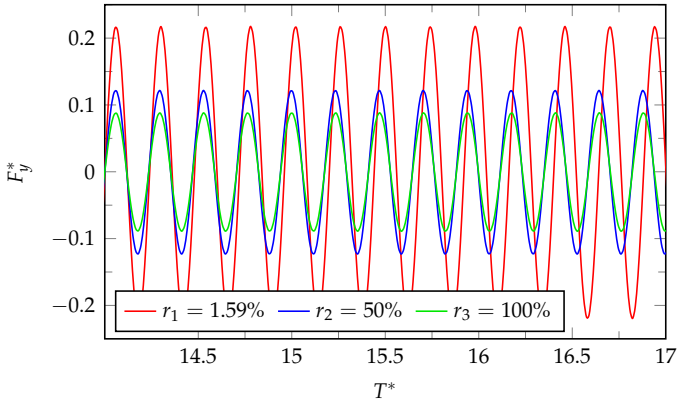

Figure 27.: Dimensionless forces developed by vortex shedding in function of dimensionless time on three fluttering plates immersed in a frontal flow with magnitude $0.35\,\mathrm{m\,s^{-1}}$. As the fillet radius increases, the amplitude decreases and the frequency increases. As we can see the trend is not linear.

amplitude and the frequency increase. However the frequency is always higher than the characteristic frequency of the motion of about 20 times.
In any case, the variability of the vortex shedding is added to the variability of both the mass and the moment of inertia, that all contribute to the dynamic of the plate. The critical zone is in the nearby to the peak points, in which small perturbations can slightly modify the plate inclination, causing macro differences in the trajectory path.

5 CONCLUSIONS

Science is built up of facts, as a house is built of stones; but an accumulation of facts is no more science than a heap of stones a house.

Jules-Henri Poincaré (1854-1912)

This chapter concludes the thesis with a brief summary of what has been done as well as the main conclusions achieved. In addition, the last part contains some suggestions for future works.

5.1 SUMMARY

In this work a two-dimensional model of falling body immersed in a fluid has been developed. The model is governed by the fluid-body interaction described by coupling the Navier-Stokes and rigid body dynamic equations. It was constructed by using the commercial software STAR-CCM+ and it is characterized by the use of the sliding mesh method: basically, it consists on a floating object fixed on an internal disk that can rotate with respect the rest of the mesh. This approach results particularly suitable for free falling object because larger rotating angles will be evolved and a fine mesh restricted only in the disk region is required. The mesh is formed by polyhedral mesh and is composed by several refinement regions. In the fluid body interface, prismatic mesh is used.The detailed model is described in Chapter 2.

The model predictions have been validated in Chapter 3 using both the experimental data obtained by [21] and the numerical results of [26]: in particular the available literature data were the trajectory (both mean values and pattern), the forces and the torque in function of the plate angle and the simulation time.

In general, numerical solutions have a certain number of input parameters that are not all well known and uncertainties can exist, introducing some uncertainties in the model outputs. In order to take into account the uncertainties, Non-Intrusive Spectral Projection (NISP) method based on polynomial chaos was used because a reformulation of the governing equations was not feasible. The study was concentrated on the one-dimensional case, and just the fillet radius of the plate corners was considered as random variable. Furthermore, it was assumed that the input parameter was characterized by a uniform PDF. The study, described in Chapter 4, was focused on finding the median trajectory and the related error bar for both tumbling and fluttering regimes. In addition, we were interested in finding the plate position interval after a specified fall.

5.2 MAIN CONCLUSIONS

Through the results obtained in this work, five principal conclusions can be drawn:

1. The adopted numerical methodology provided realistic results for two-dimensional tumbling plate and the model can correctly predict the trajectory, the forces and the torque acting on the body. The predictions are in good agreement with experimental data; results confirm and give details on how the wake is governed by a vortex shedding process.

2. In the tumbling case, the fillet corner highly modifies the trajectory mean angle and angular rotation modulus. We ascribe this fact to the different wake structure caused by the different corner sharpness, which originate different flow separation processes.

3. In fluttering, the locus of the second glide peaks displays an unexpected behaviour for r included in the interval $[0.50\frac{h}{2}\ 0.77\frac{h}{2}]$. The wake examination reveals that the vorticity field around the plate is characterized by a wake-body interaction which perturbed the trajectories.

4. In tumbling motion five points are sufficient to find correctly the solution with the NISP approach, and results show the bimodal trajectory and the increasing error bar.

5. In the fluttering regime, a much higher number of deterministic solutions is required. The system is characterized by a great variability and small perturbations in the geometry shape (input) cause large variations in the trajectory (output) underlying how the system is strongly non-linear. After the second glide, an apparently chaotic behaviour is observed that can be clarified with stochastic calculations but require a prohibit number of simulations.

5.3 FUTURE WORK

Future studied could take into account the three-dimensional case, in which more complex wake structures are involved. In addition, could be interesting to study the barks fall, in which some model parameter, like initial orientation or wind velocity, can be modelled using the NISP approach.

A DIMENSIONAL ANALYSIS

The motion of 2D plates is governed by six independent physical variables ($N = 6$), i.e. the length of the plate l, the thickness h, the fluid density ρ_f, the body density ρ_b, the kinematic viscosity ν and the acceleration due to gravity g. If we rewrite the previous quantities by using the fundamental physical units we have:

$$\begin{aligned} [l] = [L] \qquad [h] = [L] \qquad [\rho_s] = \left[\frac{M}{L^3}\right] \\ [\rho_f] = \left[\frac{M}{L^3}\right] \quad [\nu] = \left[\frac{L^2}{T}\right] \quad [g] = \left[\frac{L}{T^2}\right] \end{aligned} \tag{27}$$

As we can see, the previous parameter can be expressed using only three primary dimensions ($M = 3$), L length, M mass and T time. Now the Buckingham theorem says that the problem can be completely defined by $N - M = 6 - 3$ dimensionless groups.
At this point we have to choose three physical variables that contain, at least one time, all the primary dimensions. We choose l, ρ_f and g. The dimensionless groups are formed by taking each of the remaining parameters h, ρ_b and ν in turn, and express them in function of the chosen variable in such a way that the dimensions are conserved. Let us start with the thickness of the plate:

$$h = l^{N_1}\, \rho_f^{N_2}\, g^{N_3} \tag{28}$$

substituting the relations above (27) and rearrange the various terms, we get:

$$\begin{aligned} [L] &= [l]^{N_1}\, [M]^{N_2} [L^{-3}]^{N_2}\, [L]^{N_3} [T^{-2}]^{N_3} \\ &= [L]^{N_1 - 3N_2 + N_3}\, [M]^{N_2}\, [T]^{-2N_3} \end{aligned} \tag{29}$$

Therefore, to preserve the identity, we have to solve the follow system of equations:

$$\begin{cases} 1 = N_1 - 3N_2 + N_3 \\ 0 = N_2 \\ 0 = N_3 \end{cases} \longrightarrow \begin{cases} N_1 = 1 \\ N_2 = 0 \\ N_3 = 0 \end{cases}$$

So, from equation (28) we can get the first dimensionless parameter, which we call it AR:

$$AR = \frac{l}{h}$$

Regarding the ρ_s, the steps are exactly the same:

$$h = l^{N_1}\, \rho_f^{N_2}\, g^{N_3} \qquad \longrightarrow \qquad [L^{-3}][M] = [L]^{N_1 - 3N_2 + N_3}\, [M]^{N_2}\, [T]^{-2N_3}$$

hence

$$\begin{cases} 3 = -N_1 + 3N_2 - N_3 \\ 1 = N_2 \\ 0 = N_3 \end{cases} \longrightarrow \begin{cases} N_1 = 0 \\ N_2 = 1 \\ N_3 = 0 \end{cases}$$

The dimensionless number is the solid to fluid density ratio $\Pi = \frac{\rho_s}{\rho_f}$.
Finally we can find the third dimensionless group considering now the kinematic viscosity of the fluid ν

$$\nu = l^{N_1}\,\rho_f^{N_2}\,g^{N_3} \qquad \longrightarrow \qquad [L^2][T^{-1}] = [L]^{N_1-3N_2+N_3}\,[M]^{N_2}\,[T]^{-2N_3}$$

$$\begin{cases} 2 = N_1 - 3N_2 + N_3 \\ 0 = N_2 \\ -1 = -2N_3 \end{cases} \qquad \longrightarrow \qquad \begin{cases} N_1 = \dfrac{3}{2} \\ N_2 = 0 \\ N_3 = \dfrac{1}{2} \end{cases}$$

so, the third dimensionless number is the so called Galilei number:

$$\mathrm{Ga} = \frac{\sqrt{l^3 g}}{\nu}$$

In resume, the system is completely defined by the following dimensionless numbers:

$$\begin{cases} AR &= \dfrac{l}{h} \\ \Pi &= \dfrac{\rho_s}{\rho_f} \\ \mathrm{Ga} &= \dfrac{\sqrt{l^3 g}}{\nu} \end{cases}$$

BIBLIOGRAPHY

[1] Nicolas Sardoy, Jean-Louis Consalvi, Bernard Porterie, and A. Carlos Fernandez-Pello. "Modeling transport and combustion of firebrands from burning trees". In: *Combustion and Flame* 150.3 (2007), pp. 151–169. ISSN: 0010-2180.

[2] S.A. Ansari, R. Żbikowski, and K. Knowles. "Aerodynamic modelling of insect-like flapping flight for micro air vehicles". In: *Progress in Aerospace Sciences* 42.2 (2006), pp. 129–172. ISSN: 0376-0421.

[3] R. Â. Norberg. "Autorotation, self-stability, and structure of single-winged fruits and seed (samars) with comparative remarks on anilmal flight". In: *Biological Reviews* 48 (1973), pp. 561–596.

[4] C. W. McCutchen. "The Spinning Rotation of Ash and Tulip Tree Samaras". In: *Science* 197 (1977), pp. 691–692.

[5] D. Lentink, W. B. Dickson, J. L. van Leeuwen, and M. H. Dickinson. "Leading-Edge Vortices Elevate Lift of Autorotating Plant Seeds". In: *Science* 324.5933 (2009), pp. 1438–1440.

[6] C. P. Ellington. "The Novel AAerodynamic of insect flight: applications to Micro-Air vehicle". In: *The Journal of Experimental Biology* 202 (1999), pp. 3439–3448.

[7] H. R. L. Allen. "Experiments on the settling, overturning and entrainment of bivalve shells and related models". In: *Sedimentology* 31 (1984), pp. 227–250.

[8] C. K. Augspurger. "Morphology and dispersal potential of wind-dispersed diaspores of neotropical trees". In: *American Journal of Botany* 73.3 (1986), pp. 353–363.

[9] James Clerk Maxwell. "On a particular case of the descent of a heavy body in a resisting medium". In: *Cambridge and Dublin Mathematical Journal* 9 (1854), pp. 145–148.

[10] L.P. Mouillard. *The Empire of the Air*. G. Masson, 1881.

[11] D. P Riabouchinsky. "Thirty years of theoretical and experimental research in fluid mechanics". In: *Journal of the Royal Aeronautical Society* 39 (1935), pp. 282–348, 377–444.

[12] Paul Dupleich. *Rotation in Free Fall of Rectangular Wings of Elongated Shape*. Tech. rep. 1201. NACA, 1941.

[13] William W. Willmarth, Norman E. Hawk, and Harvey Robert L. "Steady and Unsteady Motions and Wakes of Freely Falling Disks". In: *The Physic of Fluids* 7.2 (1964), pp. 197–208.

[14] E. H. Smith. "Autorotating wings: an experimental investigation". In: *Journal of Fluid Mechanics* 50 (1971), pp. 513–534. ISSN: 1469-7645.

[15] H. J. Lugt. "Autorotation of an elliptic cylinder about an axis perpendicular to the flow". In: *Journal of Fluid Mechanics* 99.04 (1980), pp. 817–840.

[16] H J Lugt. "Autorotation". In: *Annual Review of Fluid Mechanics* 15.1 (1983), pp. 123–147.

[17] S. B. Field, M. Klaus, M. G. Moore, and F. Nori. "Chaotic dynamics of falling disks". In: *Nature* 388 (1997), pp. 252–254.

[18] Marcin Chrust, Gilles Bouchet, and Jan Dušek. "Numerical simulation of the dynamics of freely falling discs". In: *Physics of Fluids* 25 (2013), p. 044102.

[19] L. Mahadevan, William S. Ryu, and Aravinthan D. T. Samuel. "Tumbling cards". In: *Physics of Fluids* 11.1 (1999), pp. 1–3.

[20] Andrew Belmonte, Hagai Eisenberg, and Elisha Moses. "From Flutter to Tumble: Inertial Drag and Froude Similarity in Falling Paper". In: *Phys. Rev. Lett.* 81 (2 1998), pp. 345–348.

[21] A. Andersen, U. Pesavento, and Z. Jane Wang. "Unsteady aerodynamics of fluttering and tumbling plates". In: *Journal of Fluid Mechanics* 541 (2005), pp. 65–90. ISSN: 1469-7645.

[22] Kapil Varshney, Song Chang, and Z. Jane Wang. "Unsteady aerodynamic forces and torques on falling parallelograms in coupled tumbling-helical motions". In: *Phys. Rev. E* 87 (5 2013), p. 053021.

[23] Rajat Mittal, Veeraraghavan Seshadri, and Holavanahalli S. Udaykumar. "Flutter, Tumble and Vortex Induced Autorotation". English. In: *Theoretical and Computational Fluid Dynamics* 17.3 (2004), pp. 165–170. ISSN: 0935-4964.

[24] Umberto Pesavento and Z. Jane Wang. "Falling Paper: Navier-Stokes Solutions, Model of Fluid Forces, and Center of Mass Elevation". In: *Phys. Rev. Lett.* 93 (14 2004), p. 144501.

[25] A. Andersen, U. Pesavento, and Z. Jane Wang. "Analysis of transitions between fluttering, tumbling and steady descent of falling cards". In: *Journal of Fluid Mechanics* 541 (2005), pp. 91–104. ISSN: 1469–7645.

[26] Changqiu Jin and Kun Xu. "Numerical Study of the Unsteady Aerodynamic of Freely Falling Plates". In: *Comunication in Computational Physics* 3.4 (2008), pp. 834–851.

[27] B.R. Munson, D.F. Young, T.H. Okiishi, and W.W. Huebsch. *Fundamentals of fluid mechanics*. Wiley, 2009. ISBN: 9780470262849.

[28] C. Hirsch. *Numerical Computation of Internal and External Flows: The Fundamentals of Computational Fluid Dynamics*. 2nd ed. Elsevier Science, 2007. ISBN: 978-0-7506-6594-0.

[29] H. Lomax, Thomas H. Pulliam, and David W. Zingg. *Fundamentals of Computational Fluid Dynamics*. Springer, 2001. ISBN: 3540416072.

[30] J.H. Ferziger and M. Perić. *Computational Methods for Fluid Dynamics*. Springer London, 2002. ISBN: 9783540420743.

[31] H.K. Versteeg and W. Malalasekera. *An Introduction to Computational Fluid Dynamics: The Finite Volume Method*. 2nd ed. Pearson Education Limited, 2007. ISBN: 9780131274983.

[32] V. Venkatakrishnan. "Convergence to Steady State Solutions of the Euler Equations on Unstructured Grids with Limiters". In: *Journal of Computational Physics* 118.1 (1995), pp. 120 –130. ISSN: 0021-9991.

[33] S.V Patankar and D.B Spalding. "A calculation procedure for heat, mass and momentum transfer in three-dimensional parabolic flows". In: *International Journal of Heat and Mass Transfer* 15.10 (1972), pp. 1787 –1806. ISSN: 0017-9310.

[34] Dongbin Xiu and George Em Karniadakis. "Modeling uncertainty in flow simulations via generalized polynomial chaos". In: *Journal of Computational Physics* 187.1 (2003), pp. 137 –167. ISSN: 0021-9991.

[35] M.A.A. Mendes, S. Ray, J.M.C. Pereira, J.C.F. Pereira, and D. Trimis. "Quantification of uncertainty propagation due to input parameters for simple heat transfer problems". In: *International Journal of Thermal Sciences* 60 (2012), pp. 94 –105. ISSN: 1290-0729.

[36] M.A.A. Mendes, J.M.C. Pereira, and J.C.F. Pereira. "Calculation of premixed combustion within inert porous media with model parametric uncertainty quantification". In: *Combustion and Flame* 158.3 (2011), pp. 466 –476. ISSN: 0010-2180.

[37] Dongbin Xiu and George Em Karniadakis. "The Wiener–Askey polynomial chaos for stochastic differential equations". In: *SIAM Journal on Scientific Computing* 24.2 (2002), pp. 619–644.

[38] Milton Abramowitz and Irene A Stegun. *Handbook of Mathematical Functions with Formulas, Graphs, and Mathematical Tables*. National Bureau of Standards Applied Mathematics. 1972.

[39] Alan Julian Izenman. "Recent Developments in Nonparametric Density Estimation". In: *Journal of the American Statistical Association* 86.413 (1991), pp. 205–224. ISSN: 01621459.